LA-UR-17-30299
Approved for public release; distribution is unlimited.

Title: The Nature of Scatter at the DARHT Facility and Suggestions for Improved Modeling of DARHT Facility

Author(s): Morneau, Rachel Anne
Klasky, Marc Louis

Intended for: PhD Proposal
Report

Issued: 2017-11-09

The Nature of Scatter at the DARHT Facility and Suggestions for Improved Modeling of DARHT Facility

Research Proposal

Rachel Morneau

LANL Mentor: Dr. Marc Klasky

UT-Austin Advisor: Dr. Derek Haas

Contents

Proposal Statement 3
- **Goals** 5
- **Scope** 5

Background 6
- **DARHT Facility** 6
- **Test Objects** 7
  - Flat Field 7
  - FTO 7
  - Rolled Edge 8
  - AFT 8
- **Bremsstrahlung Radiation** 9
- **Compton Scatter** 10
- **Coherent Scatter** 12
- **Hydrodynamics** 13
- **MCNP, BIE, CTH** 14
  - MCNP6 14
  - CTH 15
  - BIE 15

MCNP Model of DARHT 16
- **Materials and Geometry** 16
- **Source** 17
- **Tallies** 20
- **Variance Reduction** 21

Results and Analysis 22
- **Compton Scatter Field Results** 22
- **Compton Scatter Components** 27
- **Coherent Scatter Results** 28
- **Correlated Scatter Reconstruction** 30
- **Possible Improvements to Explore** 35
- **Compton Spectrometry Modeling** 35

List of Tasks 40

Citations 44

Appendix A 46

Appendix B 51

Proposal Statement

The U.S. Stockpile Stewardship Program [1] is designed to sustain and evaluate the nuclear weapons stockpile while foregoing underground nuclear tests. The maintenance of a smaller, aging U.S. nuclear weapons stockpile without underground testing requires complex computer calculations [14]. These calculations in turn need to be verified and benchmarked [14]. A wide range of research facilities have been used to test and evaluate nuclear weapons while respecting the Comprehensive Nuclear Test-Ban Treaty (CTBT) [2]. Some of these facilities include the National Ignition Facility (NIF) at Lawrence Livermore National Laboratory, the Z machine at Sandia National Laboratories, and the Dual Axis Radiographic Hydrodynamic Test (DARHT) facility at Los Alamos National Laboratory. This research will focus largely on DARHT (although some information from Cygnus and the Los Alamos Microtron may be used in this research) by modeling it and comparing to experimental data. DARHT is an electron accelerator that employs high-energy flash x-ray sources for imaging hydro-tests. Figure 1 shows the DARHT Facility

The DARHT Facility is shown in Figure 1.

Figure 1: DARHT facility at Los Alamos National Laboratory [2].

DARHT consists of two linear accelerators (LINACS) that accelerate electrons to very high energies (upwards of 20 MeV). These high energy electrons produce X-rays by impinging onto a high-Z target which create bremsstrahlung radiation [13]. These X-rays are then used to image a hydrodynamic test. Hydrodynamic tests are experiments that use explosives to mimic a nuclear

weapon implosion. These implosions happen very quickly and involve very large areal densities, so high energy X-rays become necessary to successfully penetrate the hydrotest.

The resulting radiographic image obtained from the hydrodynamic test is then analyzed using forward modeling reconstruction techniques to find material edges and density distributions [13]. Comparisons of these results with the hydrodynamic simulations then enable evaluations of the nuclear weapon stockpile to be made.

DARHT Axis I has a single 60-ns pulse with an endpoint energy of approximately 20 MeV electrons where as DARHT Axis II has 4-pulses of 1.6 μs with an endpoint energy of approximately 17 MeV electrons [3]. A depiction of the DARHT accelerators and imaging system is presented in Figure 2.

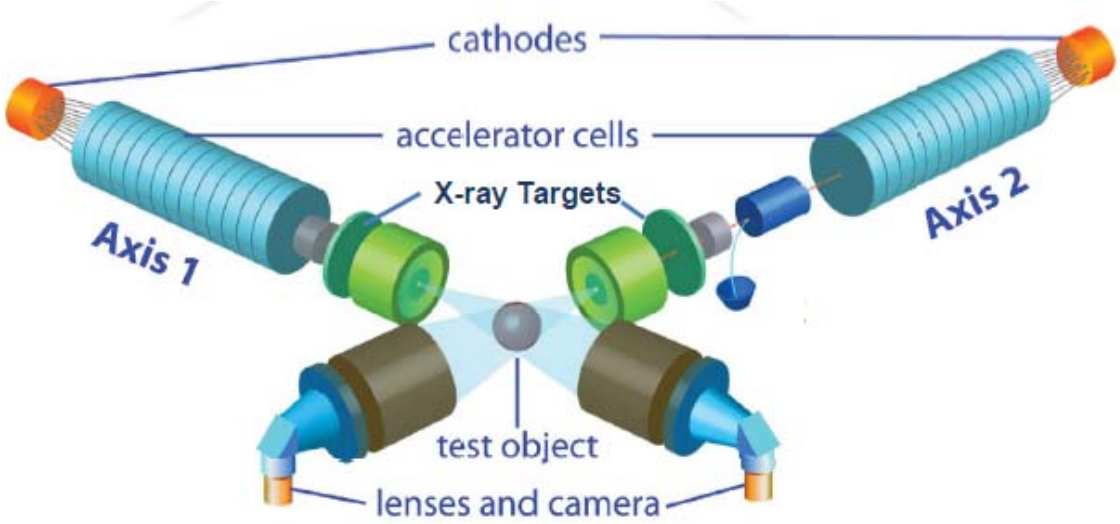

Figure 2: Diagram of DARHT facility imaging object.

Analysis of the DARHT Axis I radiographic data obtained over the past decade has demonstrated the ability to obtain excellent radiographic reconstructions. However, over this same period some difficulties have arisen in performing radiographic analyses of the DARHT Axis II radiographic data.

One difficulty encountered in the analysis of the DARHT Axis II radiographic data is the modeling of the scattered radiation. While DARHT Axis I utilizes an anti-scatter Bucky Grid to reduce the magnitude of scatter and thereby reduce errors in the density reconstructions, DARHT Axis II does not presently have such a scatter reduction device. Accordingly, the magnitude of the scatter radiation is significantly larger and thereby potentially introduces a much larger source of error in the density reconstructions. Furthermore, assumptions with respect to the curvature of the scatter field are exacerbated on Axis II due to the higher magnitude of the scatter.

Previously the Compton scatter on Axis II was believed to be fairly constant due to the large conjugates employed at DARHT [4]. (However, it was also concluded that the nature of coherent scatter could lead to significant degree of curvature on the Axis II.) Difficulties in modeling scatter at DARHT have been encountered when DARHT was initially designed [28, 29, 30, 31, 32]. Some of this was due to incomplete models [33] and insufficient computational power.

The assumption with respect to the shape of the scatter field has led to radiographic analysis models which attempt to obtain the magnitude and curvature of the scatter field in the fiducial region, exterior region of the image. In this research it will be demonstrated that this assumption is not correct and thereby necessitates a modified scatter model to infer accurate densities. Furthermore, attempts to obtain the curvature of the scatter field have led to the introduction of high order polynomials that tend to become on-separable to the density field and thereby introduce error into the inferred densities. Consequently, the focus of this research is to understand the general characteristics of scatter at DARHT and in so doing enable the development of a model that incorporates first principle physics into the modeling instead of fitting techniques. Knowledge of the scatter fields at DARHT can also enable design decisions to be made that limit variability in the end result.

Another issue associated with DARHT Axis II is the four pulses. These discrete pulses of radiation create another unique aspect. Namely, the expansion of the convertor target towards the beam and the ejection of neutral particles that are subsequently ionized and then interact with the beam and causes the defocusing of the beam. An investigation of the effect of the hydrodynamic expansion of the convertor target on the beam spectrum is also examined in this thesis.

Goals

- Develop simplified model of DARHT Axes I and II in MCNP
- Compare simplified direct model of DARHT to Bayesian Inference Engine (BIE) including source blur
- Understand nature of scatter of simplified model of DARHT Axis II
- Compare the computational model of scatter to actual DARHT Axis II data
- Explore spectral effects and effect on density reconstruction
- Develop generalized scatter model to be used in BIE reconstructions
- Develop simplified hydrodynamic model in CTH and couple with MCNP to determine effects on spectrum due to hydrodynamic movement

Scope

This research proposes to address some of the issues crucial to understanding DARHT Axis II and the analysis of the radiographic images produced. Primarily, the nature of scatter at DARHT will be modeled and verified with experimental data. It will then be shown that certain design decisions can be made to optimize the scatter field for hydrotest experiments. Spectral effects will be briefly explored to determine if there is any considerable effect on the density

reconstruction caused by changes in the energy spectrum caused by target changes. Finally, a generalized scatter model will be made using results from MCNP that can be convolved with the direct transmission of an object to simulate the scatter of that object at the detector plane. The region in which with this scatter model is appropriate will be explored.

Background

The primary objective is to understand the nature of scatter at DARHT in order to enable the reconstruction of densities. This is done with static objects instead of hydrotests (hydrotest data is classified and will thus not be in included this research but the same principles should apply). The static test objects are well known and come in a variety of shapes and areal masses which allows different information to be pulled from each and could mimic different hydrotests and regions of interest. In order to understand the nature of scatter *at* DARHT, it is necessary to understand the DARHT facility, the physics behind scatter, and the tools being used to model scatter.

DARHT Facility

DARHT stands for Dual Axis Radiographic Hydrodynamic Test. DARHT is part of the US Stockpile Stewardship Program. DARHT is an electron linear accelerator. DARHT accelerates electrons to extremely high energies.

DARHT Axis I is a single-pulse machine and analysis of the radiographic data over the past decade has led to the conclusion that it is possible to perform radiographic analysis utilizing forward modeling techniques with extreme accuracy.

DARHT Axis II is multi-pulse and presents a number of additional challenges in obtaining accurate density reconstructions due to shot-to-shot variability. It is not understood why this happens although it is likely due to beam target interactions that occur when subsequent pulses interact with ions coming off targets due to previous pulses. Some of the DARHT axes characteristics are show in Table 1.

Table 1: Characteristics of DARHT Axis 1 and 2 [12].

	Axis 1	Axis 2
Current	2 kA	2 kA
Endpoint energy	19.4 MeV	16.5 MeV
Beam pulse length	60 ns	1.6 μs
Number of pulses	1	4
X-ray pulse length	60 ns	35-100 ns
Dose	550 Rad at 1 m	Variable dose format (100-310R)

Test Objects

To characterize the performance of the DARHT radiographic system a number of objects are utilized. These objects are then analyzed to determine system performance. There are a variety of test objects that will be examined and modeled in the course of this work. Test objects are static objects that have well known dimensions and densities. Along with these test objects, there can also be tungsten plates that can be placed in the bull nose, just adjacent to the source or in closer proximity to the region between the object and source, or on either side of the object.

Flat Field

The flat field does not have any test object. Instead, the scene along the DARHT Axis stays the same and plates are added into the bull nose depending on how much areal mass is desired. Typically, in the calculations, there is 9 cm of W in the modeled flat field. This field is then utilize to remove artifacts of the imaging system from the gamma-ray camera image.

FTO

The French Test Object (FTO) is a Ta sphere surrounded with Cu and with a hole in it as seen in Figure 3. The FTO along with a graded collimator had previously been used to gather information on the scatter field by observing the intensity drop across the slot. The dimensions of the FTO are listed in Table 2. The complete schematics are in Appendix A. Finally, for the FTO, W plates may be added both in front of and in back of to provide additional areal mass. The number of plates can be varied depending on how much attenuation/scatter is desired. In some of the runs, the plates were varied from zero plates to six plates.

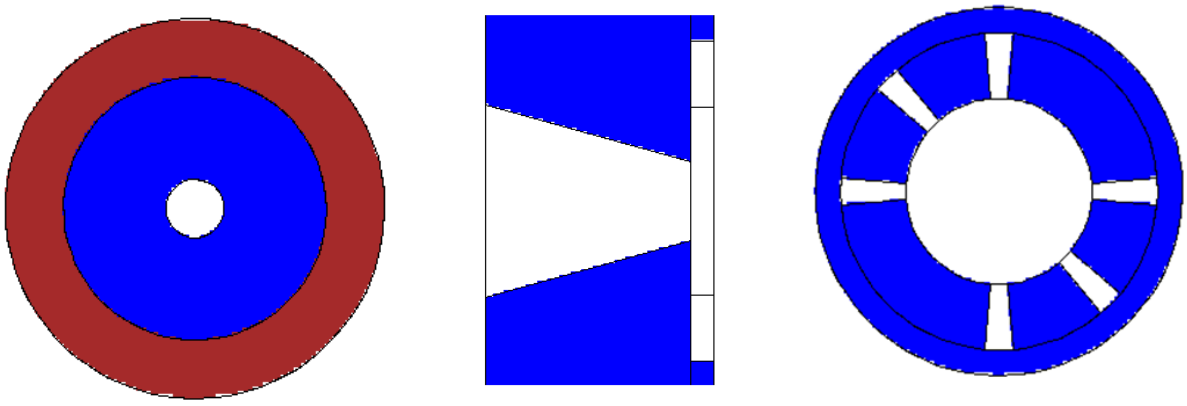

Figure 3: FTO on left, and FTO collimator (two views) on the right.

Table 2: FTO dimensions and densities.

Part	Dimension (cm)	Density (g/cm^3)
FTO – outer Cu radius	6.50	8.96
FTO – outer Ta radius	4.50	16.65
FTO – inner Ta radius	1.00	N/A

Rolled Edge

The rolled edge (seen in Figure 4) has been used to infer source blur. The rolled edge can be compared with the AFT, but under certain conditions it has been observed that the inferred blur obtained from these two test objects may differ. This is likely due to the presence of coherent scatter or correlated scatter at the image plane which is more significant in the much thicker rolled edge situation (significantly more areal mass and thus more scatter) than in the AFT case. The rolled edge has a very slight curve which the top of is in line with the center of the beam. Due to the beam being finite, it is possible to see source blur effects. However, there may be other effects contributing to what is seen at the detector plane due to the thickness of the object. There is 6 cm of W placed in the bulled nose.

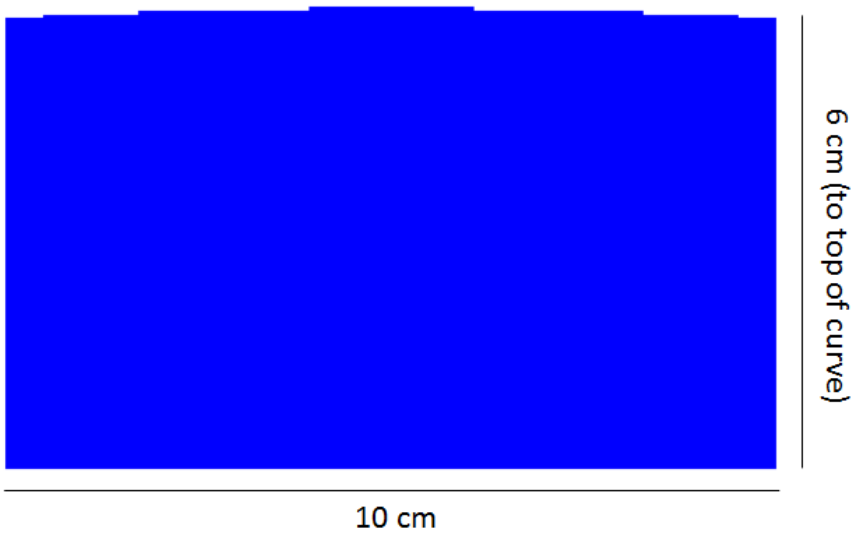

Figure 4: Rolled edge schematic, the radius on the top is 100 cm and the width is 16 cm.

AFT

The AFT (air force target) which is another object used to determine the source blur seen in Figure 5. The varying resolutions of the slots allow a source blur to be calculated from the image on the detector plane.

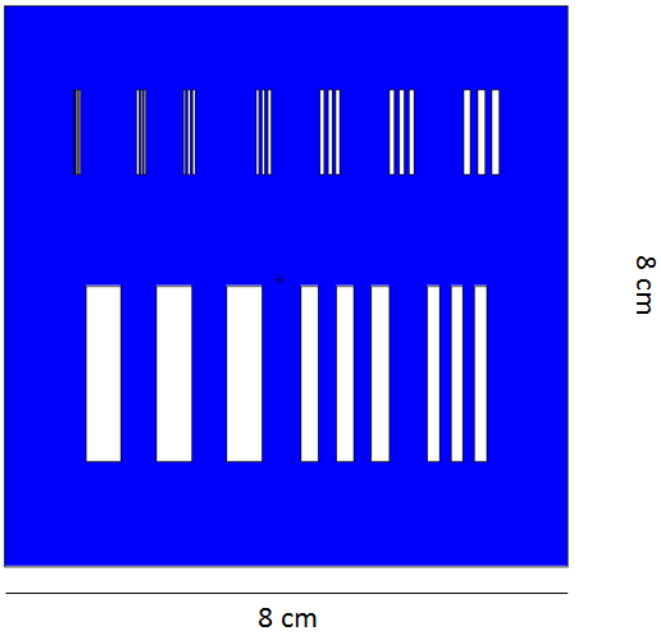

Figure 5: AFT schematic, the air force target is only 5 mm thick. The view shown is perpendicular to the beam.

More detailed schematics are available in Appendix A for all test objects except the flat field.

Bremsstrahlung Radiation

Bremsstrahlung radiation is used to image an object or hydrotest at the DARHT (and other) facilities. Bremsstrahlung (breaking radiation) is electromagnetic radiation produced by the deceleration of a charged particle when deflected by another charged particle, in the case of DARHT, an electron is deflected by a tungsten atom. The electron loses kinetic energy which is converted into a photon conserving energy seen in Figure 6.

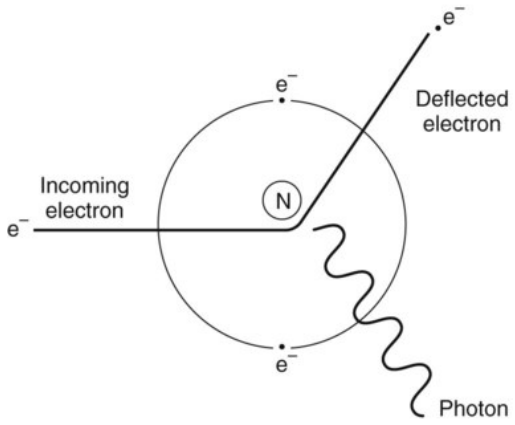

Figure 6: Picture of bremsstrahlung radiation [6].

Bremsstrahlung is continuous across energies which can be seen for the 19.4 MeV incident electron case in Figure 7. It is important to understand the beam spectrum for purposes of density

reconstruction since transmission depends on photon cross-sections which in turn rely on photon energy. As the photon beam goes through material, the spectrum will harden considerably. This is important to keep in mind, because detector response is highly dependent on the photon energy.

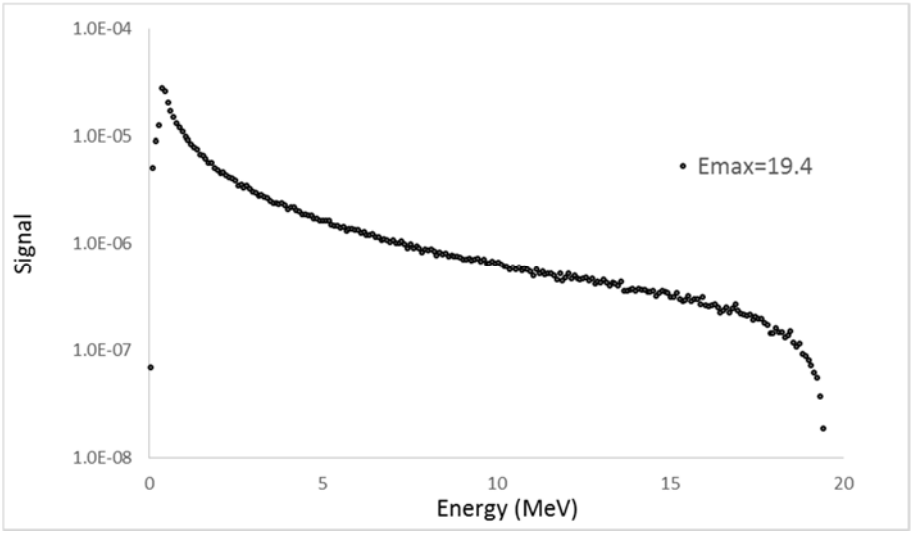

Figure 7: Bremsstrahlung photon spectrum from 19.4 MeV electron beam on tantalum.

Compton Scatter

Compton scatter is inelastic scattering of a photon by a charged particle, in our case, electrons are scattered as seen in Figure 8. The resulting scattered photon is decreased in energy and part of the photon's energy is transferred to the electron.

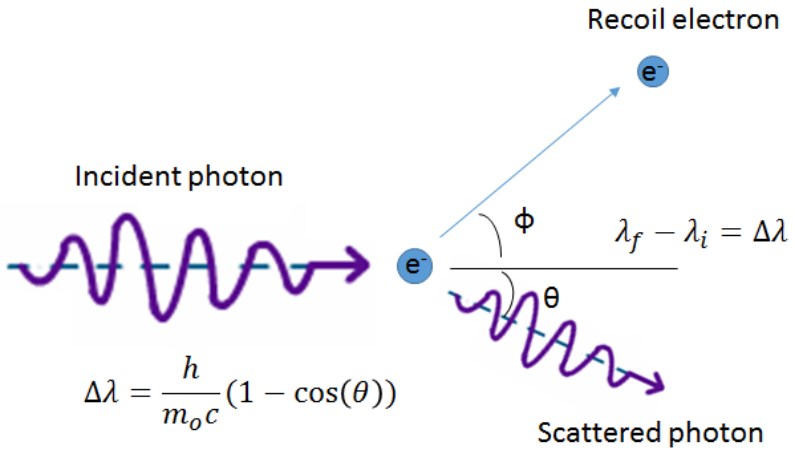

Figure 8: Picture of Compton scatter and related equations.

Compton scatter is very difficult to calculate for a system with thick areal mass while retaining information about the direction and energy of the resulting photons. This is why using the MCNP code is ideal for calculating scatter (as well as all other forms of scatter and interactions of

photons with material). Klein-Nishina describes the probability (or cross section) of an impinging photon coming off an angle. The differential cross-section is described in Equation 1.

$$\frac{\delta\sigma}{\delta\Omega} = \frac{1}{2}\alpha^2 r_c^2 P(E_\gamma,\theta)^2 \cdot \left[P(E_\gamma,\theta) + P(E_\gamma,\theta)^{-1} - 1 + Cos^2(\theta)\right] \quad (1)$$

where:

$$P(E_\gamma,\theta) = \frac{1}{1+\left(\frac{E_\gamma}{m_e c^2}\right)(1-Cos(\theta))} = \frac{\lambda}{\lambda'} \quad (2)$$

An example of this can be seen in Figure 9.

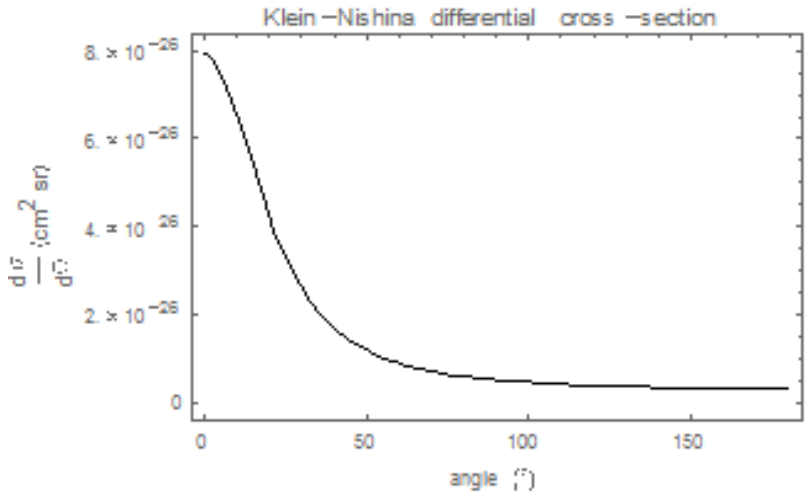

Figure 9: Differential cross section for 3 MeV photon.

Single Compton scatters are forward directed as seen in Figure 10. After multiple scatters occur, the scattered photons will be isotropic in their angular distribution. So the scatter coming off a thick object, like an FTO, is expected to be fairly isotropic. Even if it has an angular distribution, distance will tend to flatten the field as photons spread out. This result is what led people to believe that the scatter at the detector plane was also flat. This is not the case due to other materials and the long conjugates of DARHT which will be discussed in detail later.

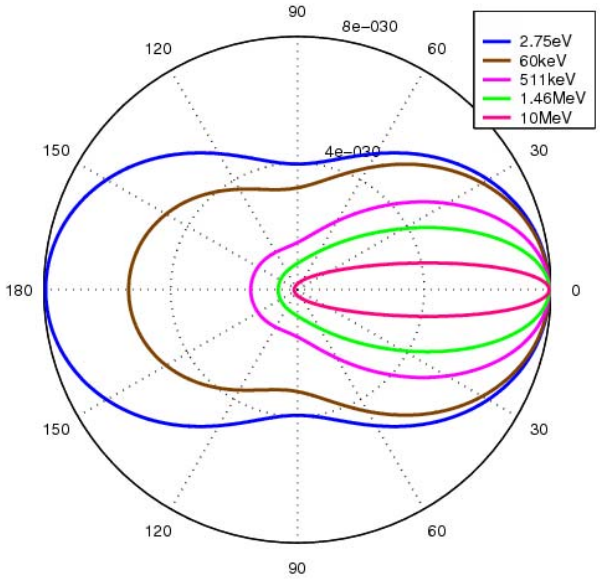

Figure 10: Distributions of scattering-angle cross sections over varying energies [5].

If only a single scatter occurs, than the scatter field begins to look like a blurred version of the direct, in other words, it is correlated to the object's characteristics. This is one of the reasons it is necessary to separate Compton scatter into two components in the BIE modeling. One component which represents isotropic scatter through a thick object and another component which represents the correlated scatter to the direct beam going through thin objects near the detection plane.

Coherent Scatter

Coherent scatter (also known as Rayleigh scattering and Thomson scatter) is another component of scatter that can be important in our calculations. Coherent scatter is elastic scatter where the photon does not change energy but changes direction. Coherent scatter varies with a relation proportional to $\frac{Z^2}{E}$ [8] where Z is the atomic number of the target and E is the energy of the incident photon. Due to the elastic nature of the scatter, the scattering angle is generally much smaller than with Compton scatter which can be seen in Figure 11. One can see that the most likely scattering angle is around 8 ° whereas Compton scatter has a more equal probability across a range of 45 ° to 135 ° at the same incident photon energy. The small scattering angle means that coherent scatter will appear correlated to an image's direct transmission, but with a blur. If the coherent scatter occurs close to the detector plane, it will not travel far from its point of origin, however, if the coherent scatter occurs far from the detector, it will have an opportunity to move away from the point of origin resulting in a correlated image at the detector plane. Unlike Compton, which will eventually spread out so much as to appear to be flat by the time it reaches

the detector, the small scattering angle of coherent will not spread out enough. At higher photon energies, scattering cross sections are dominated by Compton scatter and then pair production.

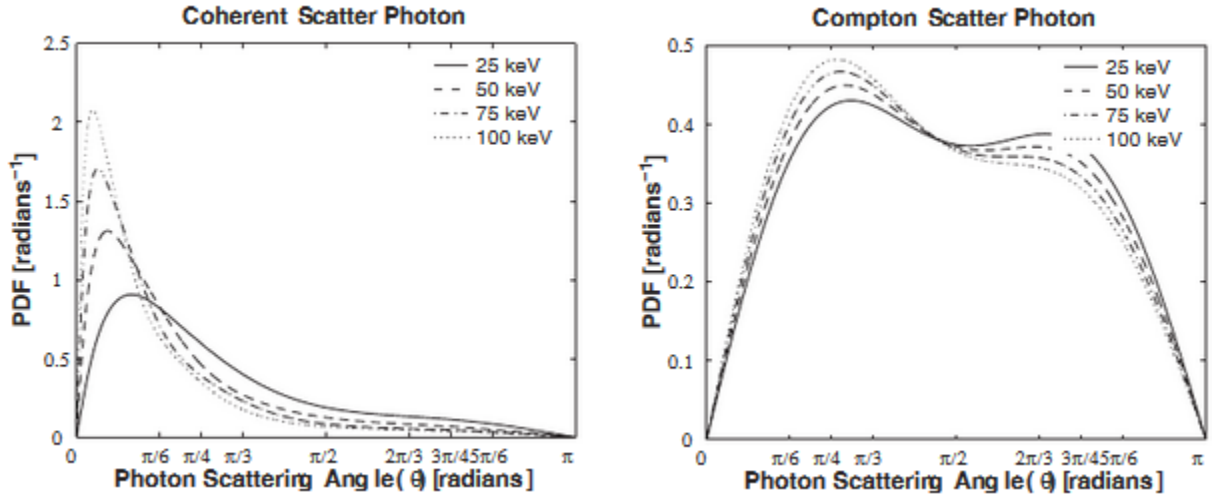

Figure 11: Photon scattering angles of both coherent scattered photons and of Compton scattered photons [9].

The coherent scatter cross-section can be described mathematically using Hubbell form factors [20]. The Thompson differential cross-section (cross-section per electron) can be described as:

$$\frac{\delta\sigma_T(\theta)}{\delta\Omega} = \frac{r_e^2}{2}(1+\cos^2\theta) \qquad (3)$$

The total cross-section of Thompson scattering from an electron is:

$$\sigma_T = \frac{8\pi r_e^2}{3} \qquad (4)$$

The coherent scatter cross-section per atom can be described as:

$$\sigma_{coh} = \int_{\theta=0}^{\theta} d\sigma_T(\theta)F(x,Z)^2 \qquad (5)$$

$$= \frac{3}{8}\sigma_T \int_{\cos 0}^{\cos\theta}(1+\cos^2\theta)F(x,Z)^2 d(\cos\theta) \qquad (6)$$

Where $x = \frac{\sin\theta}{\lambda}$ and λ is the photon wavelength in Angstoms. $F(x,Z)$ is the Hubbell form factors which are listed for different materials and values of x in [20].

Hydrodynamics

An aspect of DARHT that this research will explore is the effects of hydrodynamic movement of the target due to the interaction of the electron beam with the convertor target. The interaction of the electron beam with the bremsstrahlung convertor target causes the target material to expand and thereby reduce the effective areal mass. This has the consequence of both changing the efficiency of bremsstrahlung conversion as well as altering the photon energy spectrum.

Hydrodynamic movement of the convertor target is calculated using Euler's equations. There are three conservation equations employed. First there is the conservation of mass in equation 7.

$$\frac{d\rho}{dt} = -\rho\nabla \cdot \vec{V} \qquad (7)$$

ρ is the density, t is time, and $\vec{V}$ is the flow velocity vector. Next there is conservation of momentum in equation 8.

$$\rho\frac{d\vec{V}}{dt} = -\nabla P + g \qquad (8)$$

Where P is pressure and $\boldsymbol{g}$ represents body accelerations. Finally, there is the conservation of energy in equation 9.

$$\rho\frac{dE}{dt} = -P\nabla \cdot \vec{V} \qquad (9)$$

Using equation-of-state (EOS) data and constitutive models, these equations can be solved to solve for density, temperature, etc. from a material that has ablated due to a large amount of energy being imparted into it very quickly (or other hydrodynamic problems, but this is the one of interest for the DARHT target).

Simulation Codes

In order to properly model the physics of the beam interacting with the convertor target to generate bremsstrahlung radiation at DARHT as well as the nature of scatter at DARHT, a variety of codes will be employed that will capture photon/electron transportation, energy deposition, and hydrodynamics. In addition, to obtain the density from the radiograph a forward modeling approach is utilized. This forward modeling approach is implemented in the Bayesian Inference Engine. The following section briefly describes the computer codes utilized in this research.

MCNP, BIE, CTH

MCNP6

To describe the generation of the bremsstrahlung radiation produced in the convertor target as well as the passage of the radiation through the test objects accurate electron and photon transport models are needed [13]. MCNP6 (Monte Carlo N-Particle) is a transport code that can simulate the behavior of electrons and photons in materials. This technique will be utilized to generate both the bremsstrahlung source as well as the radiographic images.

MCNP has many capabilities; it will primarily be used to tally (count) photons and electrons at desired locations. It can provide this count in a variety of ways (flux, fluence, total number of particles, energy deposition etc.) MCNP6 can also provide electron and photon energy depositions in a material, which is utilized in this research to generate the material heating in the convertor target which will drive the hydrodynamic movement of the convertor target.

CTH

To model the hydrodynamic movement of the convertor target due to the electron heating during the four DARHT pulses the CTH hydrodynamic code will be utilized. CTH is a multidimensional, multi-material, Eulerian hydrodynamic code for solving the Euler equations [23].

Within a very short, energetic burst of electrons into a target, the target will ablate and some of the material will be ejected from the target. For a single pulse, the material will not move until after all the energy (i.e. after the duration of the pulse) has been deposited and the photons from bremsstrahlung are produced. Thus the radiographic image will not be effected by the ablating target. For multi-pulse machines, it becomes possible for the material coming off the ablated target to interact with the incoming beam of the next pulse. This will take two distinctly different forms. In the first form the energy of the beam will create desorption of neutrals that in turn give rise to ionized particles that may interact with the beam and thereby affect the focusing properties of the beam. This may in turn cause the characteristics of the spot to change and consequently effect the radiographic image. In the second case the energy produced by the electron beam may cause heating and subsequent hydrodynamic movement of the convertor target which may affect both the efficiency of the conversion of the electrons into photons due to the change in the areal mass of the convertor target over the course of the beam pulse as well as the energy spectra of the resulting photon source. In either case however, it is important to understand both the beam heating and hydrodynamic behavior. That is, in the former case the hydrodynamic behavior will serve as the initial conditions for the positive ion source which can be modeled with PIC (particle-in-cell) codes which will show the effect on charged particles. This is expected to have a larger effect on a DARHT experiment since this can possibly cause the location and size of the beam spot to change. This dissertation work will not inspect these interactions, but ideally the hydrocode results will allow further investigation into this arena. CTH was specifically chosen, because this is one of the hydrodynamic codes employed at LANL. It allows multi-dimensional analysis and can be parallelized. LANL is quite strict on the codes it allows to be used on its institutional computers and CTH is available allowing what could be a prohibitively long runtime to become feasible. CTH is also more user-friendly than RAGE, the other standard hydrocode at LANL, which is a multidimensional, multi-material Eulerian hydrocode which solves Euler's equations coupled with the radiation diffusion equation [10]. The target will ablate in multiple directions and a 2D model would appropriately capture the impact of the ablation on subsequent pulses, however, a 1D code would be insightful and this is where the research will look initially. If there is time, the 2D model will be inspected. Finally, due to the complex equations that are being solved and the potentially fine mesh needed to capture the behavior of the target, the code must be parallelized so that run times are not prohibitively long.

BIE

The BIE (Bayesian inference engine) allows actual experimental data to be analyzed. It can be used to determine information about the spot size, the nature of scatter, and many other important aspects of the shot. It should be used carefully, because it allows many variables to be optimized upon (often necessary with such a complex system); this can also provide results that

are misleading so they should be weighed as best as can be managed against the physics (true for the other codes as well). The BIE is currently being benchmarked for the experiments using data produced by MCNP, some of these results will be discussed in the thesis. The BIE is much faster than MCNP and can provide the same data as MCNP for certain cases, such as direct radiation. The BIE model of DARHT is being compared to the MCNP model of DARHT which is providing data on how to make it better. Although the model is generally only appropriate for one test object (or test objects of similar areal mass and location), shots at DARHT are constantly repeated and small changes can be made to the BIE to provided analysis rather than rerunning the much more computer intensive MCNP calculation. Using what is known from MCNP also allows certain data about an experiment to be inferred more accurately and with less optimizable variables in the BIE. The BIE can take what is known about the direct and scatter fields and use this to find a source blur for instance.

MCNP Model of DARHT

Materials and Geometry

A radiographic model was constructed using MCNP6 for the nominal DARHT Axis 2. This model can also be utilized for the recently fielded DARHT Axis 1 without the Bucky Grid. This model captures materials in the line-of-sight, i.e. materials that fall within the 2.55 ° half-angle cone starting at the source. The materials in the line of sight can be seen in Appendix A for the flat field, FTO, rolled edge, and AFT set ups. Individual areas are broken up into smaller areas with materials and thicknesses denoted. In Table 3, the line-of-sight materials are denoted. It should be noted however that there are some materials that are outside the line-of-sight that were incorporated into the model. It is expected that photons that scatter off line-of-sight materials have the potential to scatter back from surrounding materials into the line-of-sight. Only a few materials were added to capture some of this effect (such as the GRC and CV). This simplified model, while not attempting to include all of the materials outside of the line-of-sight, is meant to elucidate the pertinent physics. Consequently, in comparing the simulation with the actual radiographic data some deviations from the experiment may be expected to exist. Treatment of these anomalous effects is also included in this thesis research.

The table below and the figures in Appendix A depict the geometry that was incorporated into the MCNP simulation model. This is the base for all subsequent MCNP runs. A line-of-sight schematic from the DARHT facility is also attached to Appendix A.

Table 3: Line-of-sight materials not including test objects.

Parameters			Flat Field	FTO	Rolled Edge	AFT
Line-of-sight	Materials	ρ (g/cm^3)	Thickness (cm)	Thickness (cm)	Thickness (cm)	Thickness (cm)
Be window	Be	1.827	0.48	0.48	0.4780	0.48

Compton diode	Al	2.713	0.52	0.52	0.5207	0.52
Entry cover window	Al	2.823	0.63	0.63	0.6350	0.63
Entry window	Al	2.823	5.08	5.08	4.4450	5.08
B4C disk	B4C	2.519	0.95	0.95	0.9500	0.95
W slabs	W	19.25	9.00	n/a	6.5000	9.00
Object			n/a	FTO	RE	AFT
CV B4C disk	B4C	2.519	2.39	2.39	n/a	2.39
CV Al exit window	Al	2.713	5.08	5.08	n/a	5.08
SV port cover		1.19	n/a	n/a	0.6350	n/a
GRC port cover	Al	2.713	0.32	0.32	0.3175	0.32
Bucky grid cover	Al	2.713	n/a	n/a	0.0880	n/a
Camera enclosure	Al	2.713	0.14	0.14	0.1397	0.14
Scint. outer cover	Al	2.713	0.33	0.33	0.3302	0.33
Scint. back clamp	Al	2.713	0.38	0.38	0.3810	0.38
Ta sheet	Ta	16.65	0.05	0.05	0.0510	0.05

Source

In addition to the specification of the geometric configuration to be simulated, the MCNP model incorporates the source photon energy spectrum and source spot in the simulation. The photon energy spectrum for the subsequent radiation transport was obtained by first modeling the interaction of a monoenergetic electron with the convertor target.

Specification of the electron source is simple, it is a point source located at the origin as shown by the keyword POS. The PAR keyword is set to 3, indicating electrons. ERG is set to the electron endpoint energy: using 19.4 MeV (DARHT Axis 1) or 16 MeV (DARHT Axis 2). Finally DIR and VEC indicate that the source is monodirectional and the direction it travels respectively.

SDEF ERG=19.4 POS=0 0 0 PAR=3 DIR=1 VEC=1 0 0

The geometry specified for the determination is a simple slab of 1 mm thick Ta. A F4 tally with energy binning was utilized to determine the energy spectrum. The resulting spectrum can be seen in Figure 12.

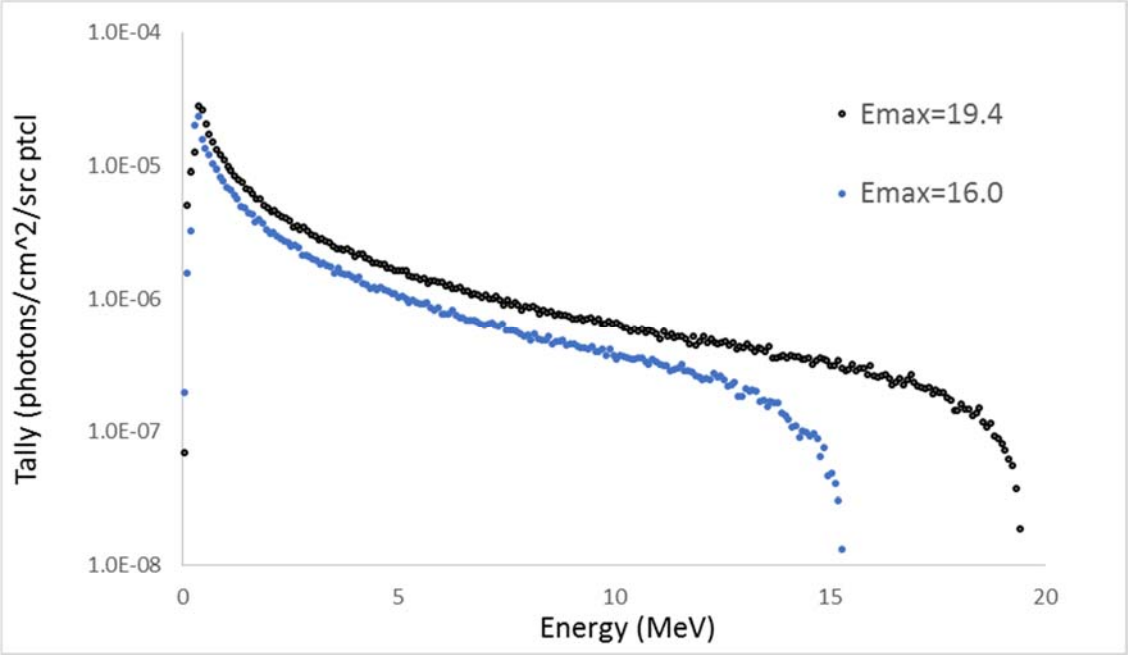

Figure 12: Bremsstrahlung spectra for DARHT Axis 1 and Axis 2.

These photon spectra are utilized in the subsequent radiation transport calculations via the specification of the photon energy spectra as follows.

SDEF ERG=D3 PAR=2
SI3 $E_1 \cdots E_n$
SP3 $P_1 \cdots P_n$

D3 denotes that distribution 3 characterizes the energy spectrum, SI3 gives each energy bin and SP3 gives each probability associated with the energy bin. PAR is set to 2 which indicates that the particles from the source are photons.

The photons emitted from a bremsstrahlung source are within in a finite cone of 2.55 ° [7]. This is accounted for in the source definition using the DIR keyword and a distribution as shown in the MCNP lines below. The direction is inputted as the cosine of the angle.

SDEF ERG=D3 PAR=2 DIR=D2
SI2 -1 0.99901 1
SP2 0 0 1

It should be noted that the dependency of the photon energy spectra variation as a function of angle emitted from the Ta convertor has been demonstrated to be negligible and consequently was ignored.

Finally, the energy spectrum was benchmarked using a Compton spectrometer as discussed in the Compton Spectrometry Modeling section.

A crucial element in the development of the forward radiographic model is the determination of the source blur. Historically, the source blur is inferred using the BIE from one or more of the following resolution targets: AFT, circular resolution target, pin hole, or the rolled edge. An example inferred spot from DARHT is provided in Figure 13.

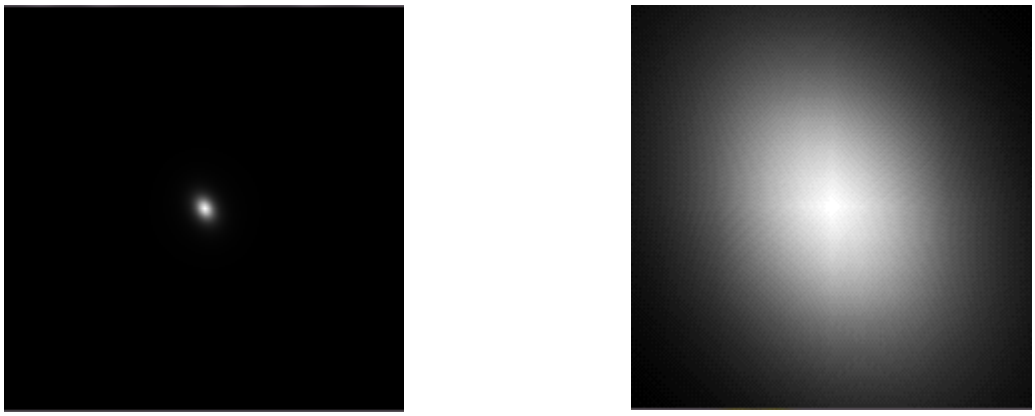

Figure 13: Image of PSF spanning entire range inputted on the left and showing a close up on the right.

To illustrate the very localized nature of the PSF a line-out of the PSF is provided in Figure 14.

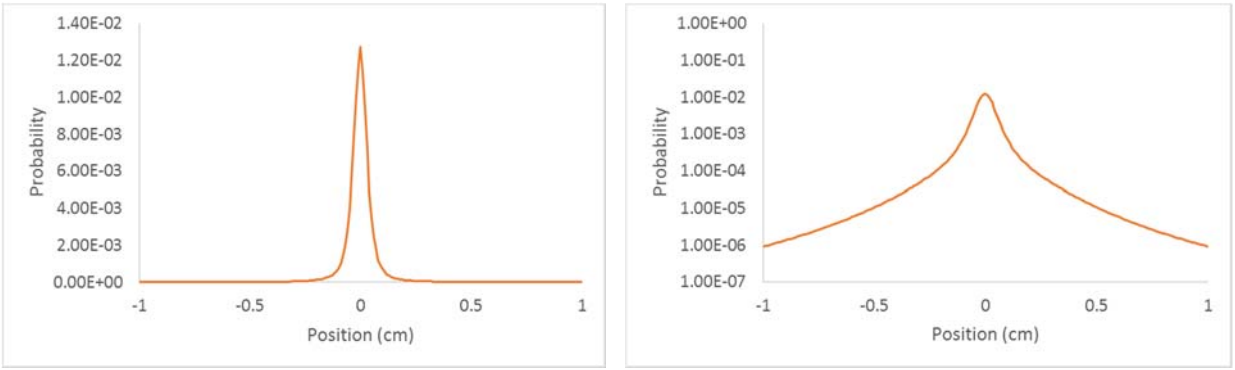

Figure 14: Lineout of source PSF, linear scale on left and log scale on right.

It should be noted that the BIE utilizes this blur to convolve the uncollided flux in the forward model. In this research, the validity of this approximation is examined by simulating the image formed via the direct radiation with a finite spot. This approach does not suffer from the limitation of convolving with a blur kernel at a single location. Detailed comparisons with the previous approach will be performed and an alternative convolution model will be developed to improve on the current method.

The specification of the finite source with MCNP requires that the source intensity and position be specified using the following options:

SDEF POS=D4

Where D4 is the PSF, the SI4 card will hold positions in the form of x_1 y_1 z_1 and the SP4 will have the probability of emission from that point.

A source bias card (SB4) is utilized which allows the source to be sampled sufficiently without having to run a huge number of particles since the PSF spans almost six orders of magnitude as seen in Figure 14. The biasing card allows MCNP to split (or multiply) particles at a certain position of low probability while simultaneously lowering the importance of the particles produced so that the overall tally is the same wherever the particles are counted. The bias used for the PSF is:

$$bias(x) = \frac{1}{PSF(x)^{0.25}}$$

The source must be sufficiently sampled in order to have accurate results. Although the results may indicate in MCNP that the problem is converged due to small statistical uncertainty, it does not explicitly take into account the sampling of the source. In order to ensure the source is sampled sufficiently, MCNP provides a means of demonstrating adequate sampling has occurred. This is illustrated by comparing the number of particles emitted from the source with the expected number of source particles. In Figure 15, the data from MCNP is plotted showing that the source is sampled very well in both energy and position.

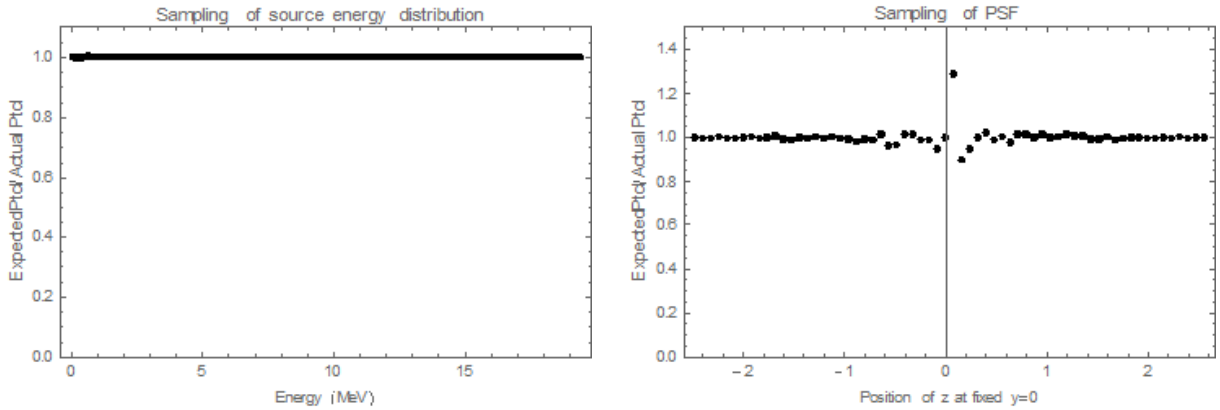

Figure 15: Source sampling of energy on left and source sampling of position on right.

Tallies

The last component of the MCNP model is the tally. Tallies are chosen depending on the information required. For the most part, the flux at the detector plane is required. Some of the tallies that will be used are F4 tallies which calculate the flux in a specified volume (this could be the detector volume), F1 tallies which count particles crossing a plane, F3 tallies will calculate energy deposition in a volume, and F5/FIR tallies which are radiography tallies. The radiography tallies are of special importance since they allow the components of the photon (direct and scatter) to be separated from each other. F4 tallies calculate the entire photon flux in a volume whereas the radiography tally can be specified to tally just direct flux (photons that do not scatter

at all) and the scatter flux (photons that scatter at least once). It is then possible to further separate Compton scatter from coherent scatter by turning off the coherent scatter on the PHYS card and tallying just Compton scatter. It is possible to obtain only the coherent scatter by tallying only scatter but also introducing a CUT card for the photon energy. However, in this case one must utilize a monoenergetic photon. That is by running monoenergetic photons and setting a CUT card to be only slightly lower than the source photon, it is possible to tally the coherent scatter by itself. In this manner, Compton scattered photons, will be removed due to the energy loss and accordingly will not contribute to the tally. By examining a series of discrete photon energies one can obtain an estimate of the coherent scatter. It should be noted that this approach provides an estimate of the single scattered coherent scatter which is precisely what is desired. That is, while additional photons undergoing other interactions may also ultimately undergo coherent scatter they will no longer be correlated directly with the un-collided signal.

Variance Reduction

It is necessary to employ a variety of variance reduction techniques in order to sample the source adequately as well as get decent statistics at the image plane. Already discussed were the BIAS card in the source definition as well as the BREM card in the bremsstrahlung simulation. The BIAS card allows the probability of a particle at a certain energy and position to be increased while adjusting the weight of that particle accordingly. The BREM card increases the probability of photons at higher energies being emitted by bremsstrahlung while decreasing the weight of those photons as well. To get good statistical uncertainty at the image plane in MCNP, it is necessary to use weight windows. These weight windows will also ensure that the scatter field is adequately sampled by increasing the importance of photons going through materials while adjusting the weight of the photon. A mesh is created in MCNP dividing the geometry in such a weight that photons going through a material can be given a new importance based on the pixel they enter. It is desirable to mesh the material containing geometry more finely than empty space. A point detector is placed at the detector plane so that MCNP knows to optimize the weight windows with respect to a tally at the image plane. Once a set of weight windows is generated, it is possible to put these weight windows back into MCNP and allow it to optimize the weight windows again. The final weight windows for an FTO with four plates can be seen in Figure 16.

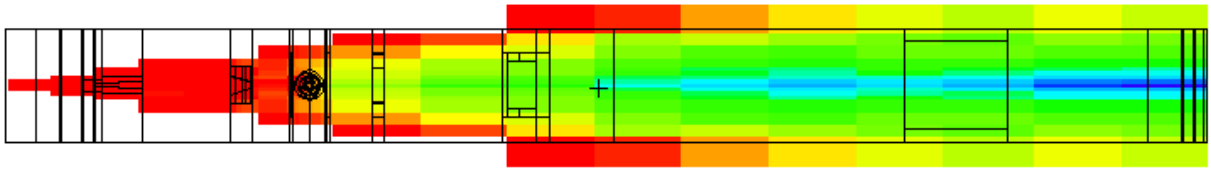

Figure 16: Weight windows generated by MCNP for DARHT FTO with 4 plates. Blue indicates that particles are more likely to reach detector plane.

Results and Analysis

In the following sections, some illustrative results of the work that has been performed are presented.

Compton Scatter Field Results

Due to the nature of the scattered radiation, diffuse in nature, the radiographic tally was utilized to separate scatter from direct for a number of test objects. As previously discussed, the radiographic tally does not retain subpixel information due to the nature of the tally; however, this information is not required due to the much larger spatial scale of scatter. The first scatter fields that are shown are from the AFT with a 19.4 MeV bremsstrahlung source. For detector placement refer to Appendix A which shows the locations with respect to materials in DARHT. Materials and their dimensions can be found in Appendix A.

Measurements of the Compton scatter field are presented at different locations along the axis to observe the evolution of the Compton scatter field as the radiation proceeds to the image plane. At the detector plane (which is at 525 cm, but the detector has been placed 1 cm away from it to avoid issues encountered when radiographic tallies are placed too close to a scattering material), the scatter field appears to be quite flat. This is consistent with previous radiation transport models for the scatter field for all objects at DARHT; however, when looking at the FTO, it becomes clear that this is not true for all objects.

Details of the evolution of the scatter for the AFT are presented in Figure 17-18. The thickness of the AFT, 3 mm, combined with the large distance from the image plane (391.7 cm) produces a scatter field at the detector plane that is very flat as seen in Figure 19. There is some shape that can be seen right after the AFT (see Figure 17 at 135 cm), but this quickly diffuses producing a very flat field, again. Some modulation in the scatter field may also be observed in the scatter field at 241 cm (see Figure 18) due to a 5 cm Al plate. The modulation in the scatter field in close proximity to the Al plate occurs due to the impact of the uncollided (direct) photons hitting the Al plate and scattering. Again, the modulation quickly flattens out as may be observed at the 470 cm location.

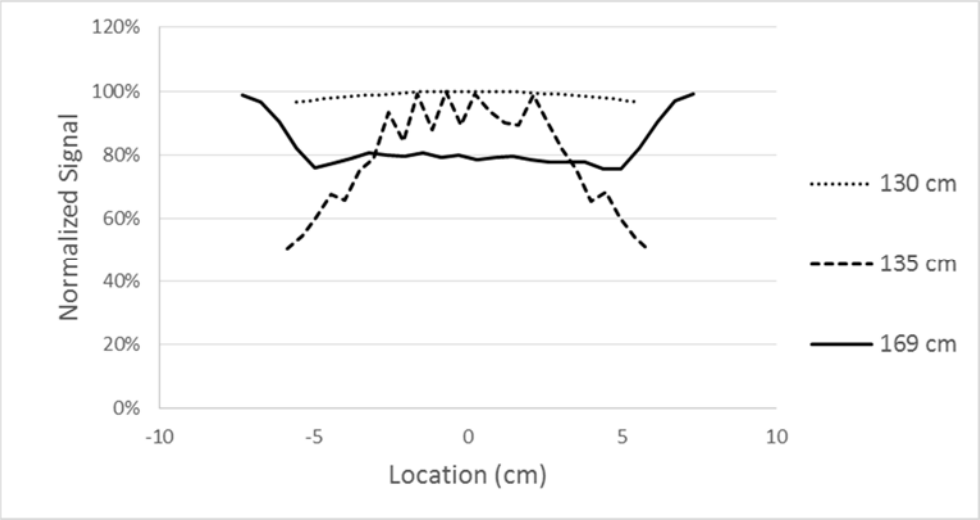

Figure 17: Scatter fields of AFT at various locations with 6 cm of W in bull nose.

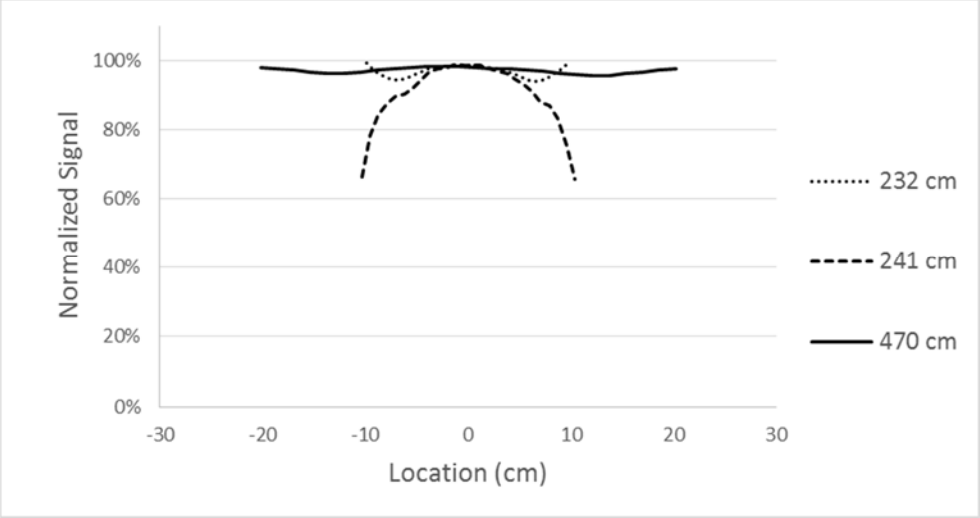

Figure 18: Scatter fields of AFT at various locations with 6 cm of W in the bull nose.

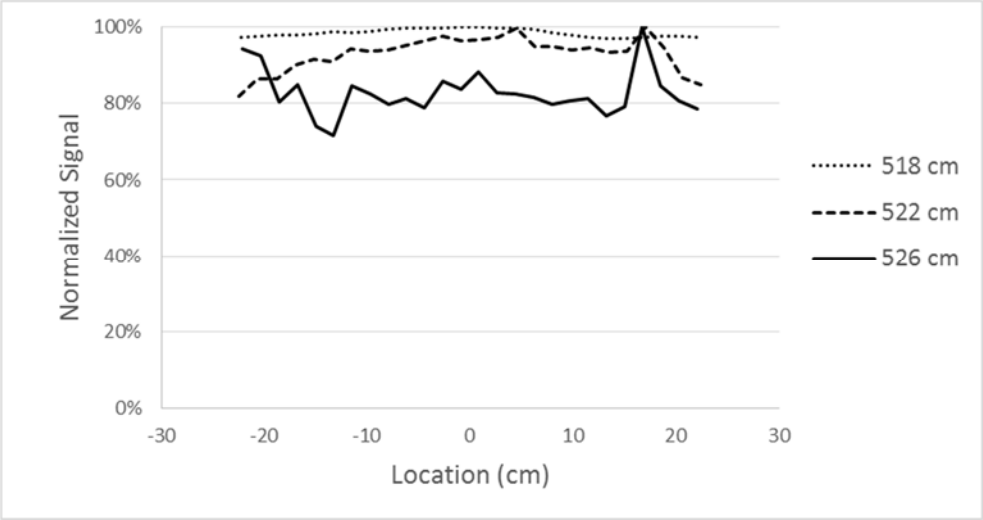

Figure 19: Scatter fields of AFT at various locations with 6 cm of W in the bull nose.

As previously discussed a number of resolution targets are utilized at DARHT to infer the source blur. The rolled edge is another radiographic object that is utilized to this end. Previous investigations have indicated however that the inferred spot size differed when utilizing the rolled edge. Consequently, transport simulations of the rolled edge have been performed to elucidate the difference between the rolled edge and the AFT inferred blur. Preliminary, results indicate that the differences are attributed to both the correlated scatter due to the aluminum plates in proximity to the image plane as well as the coherent scatter.

Simulations have also been performed on the FTO. These results are much more informative with respect to elucidating the nature of scatter at DARHT on Axis II. The scatter field of the FTO is more interesting, as can be seen in Figure 20, Figure 21, and Figure 22.

As has been previously discussed the transport of radiation proceeds in a manner analogous to that described for the AFT. This may be observed from examination of Figure 20, Figure 21, and Figure 22. It should be noted that the modulation of the scatter following the aluminum window is more pronounced than was observed for the AFT. This is because scatter is produced from the direct photons (which are more peaked due to a larger intensity step in the FTO relative to the AFT) hitting the window and scatter from the object (which is flat) is absorbed. As with the AFT, the scatter following the aluminum window flattens. In Figure 21, wings begin to appear on the 395 cm scatter field. This is due to the large amount of scatter created at the object, some of that scatter can be reflected by surrounding materials that are not hit by the direct transmission. The reflected scatter causes sharp wings to be seen on the edges of the scatter field. These wings become even more prominent closer to the detector as can be seen in Figure 22. In Figure 22, it is obvious that the scatter field is no longer flat. There is almost 40 % modulation in the scatter field as well as what appears to be shape correlated to the FTO direct transmission, which is seen in Figure 23. It will be shown that this correlated shape is due to materials (windows) placed very closely to the detector. Not only is the scatter field no longer flat, it can no longer be simply defined since it has a constant component due to scatter at the object plane and a correlated field due to scatter from the materials close to the detector.

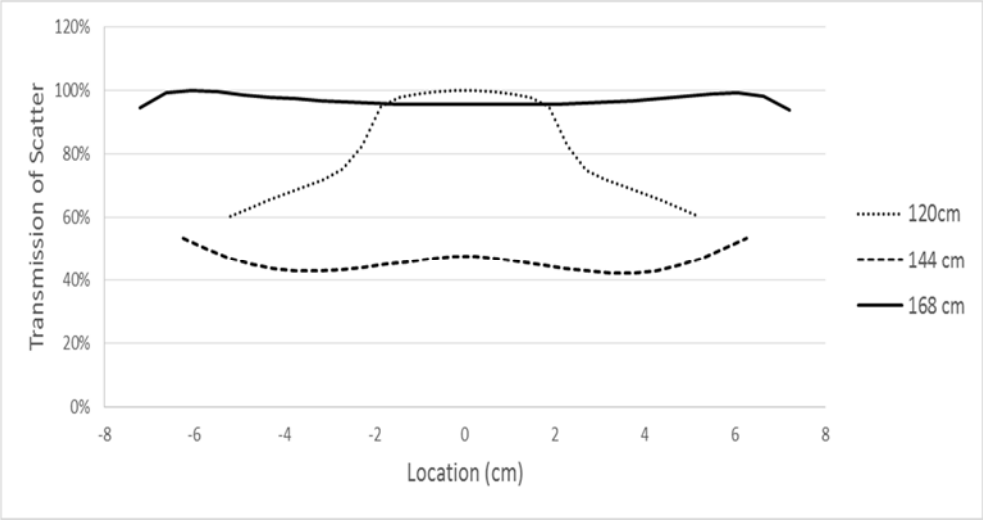

Figure 20: Scatter fields of FTO at various locations with 2 cm of W on either side of the FTO.

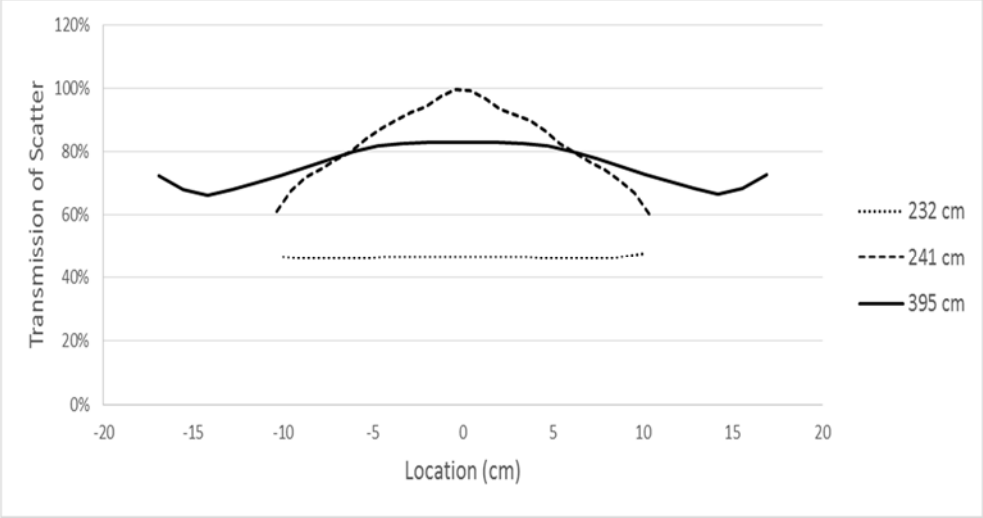

Figure 21: Scatter fields of FTO at various locations with 2 cm of W on either side of the FTO.

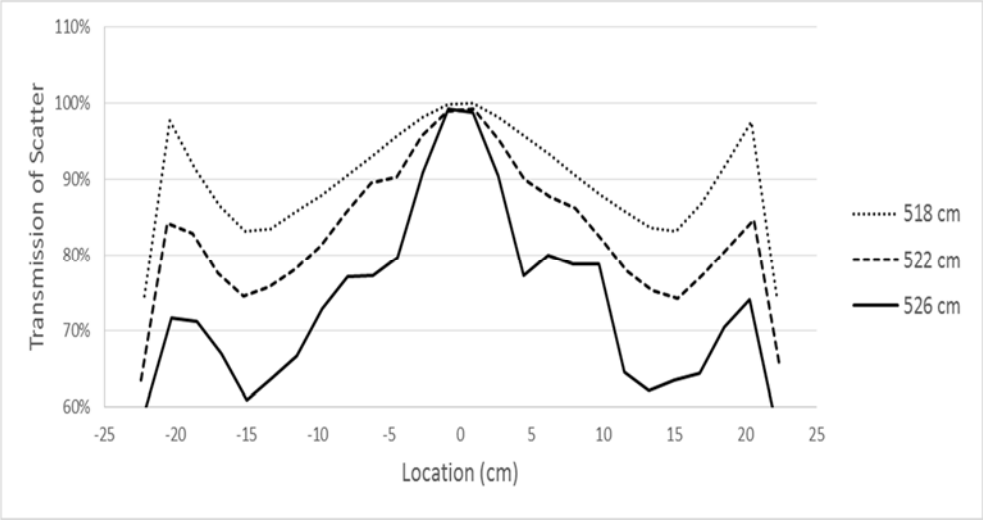

Figure 22: Scatter fields of FTO at various locations with 2 cm of W on either side of the FTO.

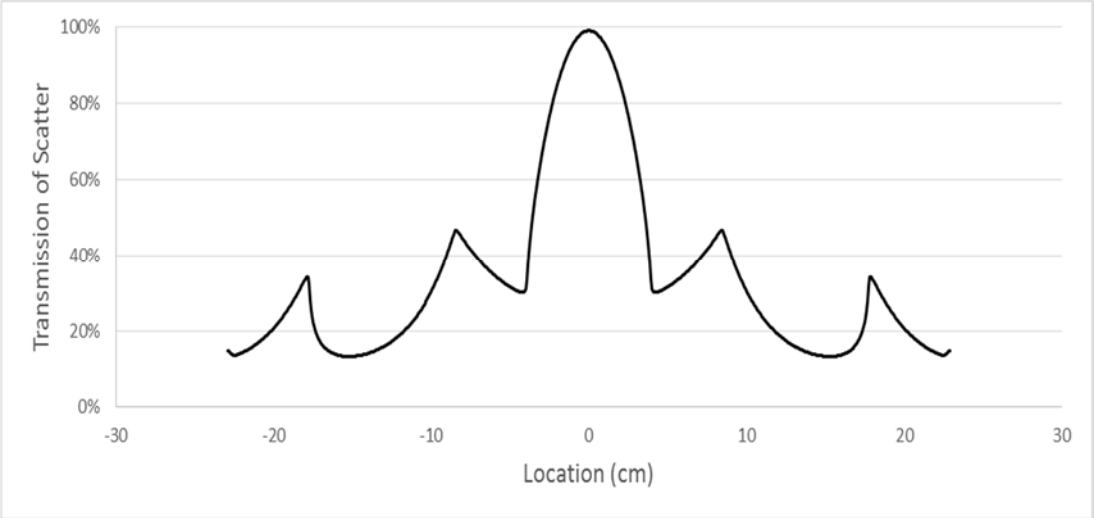

Figure 23: Direct transmission of FTO at detector plane with 2 cm of W on either side of the FTO.

Knowledge of the magnitude of the scattered radiation relative to the direct signal is also of interest. The scatter-to-direct ratio will be used later to compare the correlated scatter to non-correlated scatter and can also be utilized to gauge the consistency of the inferred scatter magnitude obtained via the BIE with radiation transport calculations. The scatter-to-direct ratios are presented for the FTO in Table 4.

Table 4: Scatter-to-direct ratios for FTO with different number of plates around it.

Position	0 Plates	2 Plates	4 Plates	6 Plates
On Axis	0.080	0.084	0.130	0.203
Off Axis	0.311	0.385	0.537	1.098

Having performed radiation transport simulations on a variety of object it is now instructive to examine from a physics perspective the constituent components so as to both aid in the interpretation as well as to facilitate the development of a general scatter model that may be implemented into the BIE.

Compton Scatter Components

Compton scatter as given by the Klein-Nishina relationship produces both a down-scattered photon which can undergo another radiation interaction (bremsstrahlung, annihilation radiation, etc.). As may be observed from Figure 20, Figure 21, and Figure 22 the diffuse nature of the scatter law tends to produce a relatively flat field as one moves away from the scattering source. By performing a series of simulations with the FTO with 4 plates and removing the scene and adding parts back into it, such as the camera plate, the origin of the modulation of the scatter at the image plane is isolated. From examination of Figure 24, it is obvious that the modulation in the scatter field is due to the camera plates. The scatter field is very flat when there is no scene, just the four W plates and FTO (as well as FTO collimator). Furthermore, when materials before the FTO are incorporated (rough collimator, diodes, etc.), the scatter field is still quite flat. However, inclusion of the camera plates produces a modulated scatter field. The scatter field instead looks like a blurred version of the direct as seen in Figure 25.

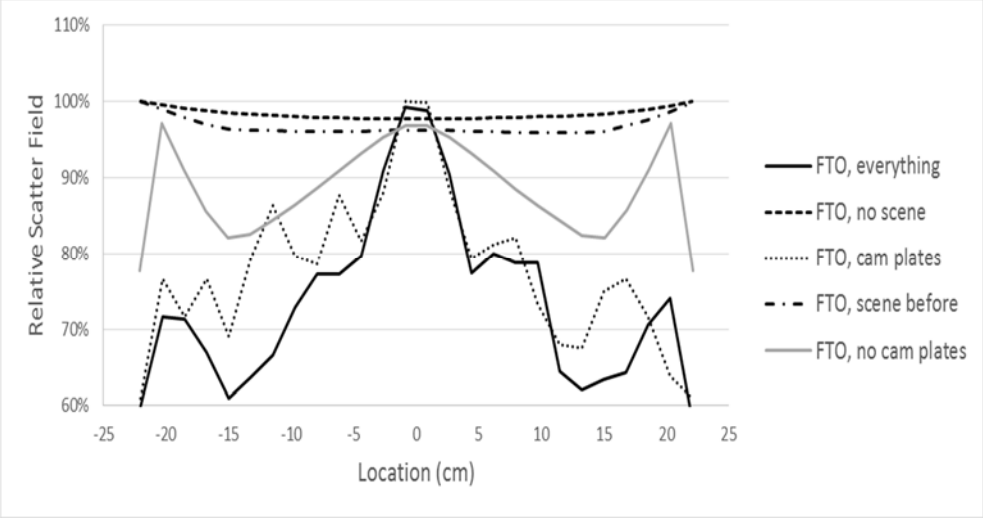

Figure 24: FTO with 4 plates (2 cm of W on either side) with varying scenes.

Figure 25 indicates that the scatter field is a blurred direct signal. This modulated scatter field arises due to the direct photons interacting with the near detector plates and causing a significant number of single Compton scattering interactions to cause an effective blurred image. Furthermore, because the scattering source is in close proximity to the image plane there is not sufficient distance to allow the scattering field to diffuse and become flat.

One additional point worth discussing, the effect is only apparent when the fraction of the correlated scatter is comparable to that of the Compton scatter arising from interaction of the beam with the object. Furthermore, as may be observed from examination of the scatter from the AFT, there must be sufficient modulation in the primary object otherwise the modulation in the

scatter from the near field plates will be almost negligible. This later instance may be observed from the AFT seen in Figure 19.

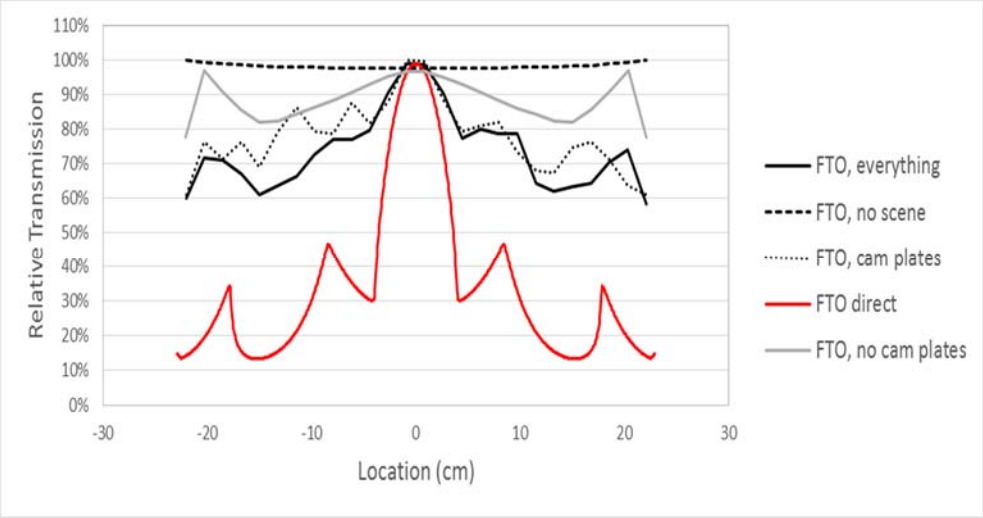

Figure 25: FTO scatter fields compared with FTO direct field.

Coherent Scatter Results

Although the cross-section for coherent scatter is very low, the appreciable areal masses encountered at DARHT in conjunction with the large distance from the object to the image plane leads to a rather large fraction of the coherent scatter relative to the Compton scatter to be present at the image plane. In a manner similar to the correlated Compton scatter created by the interaction of the uncollided flux with the materials in close proximity to the image plane, the coherent scatter will also create a blurred image of the object that is being imaged. Figure 26 shows the total correlated coherent scatter field found in MCNP.

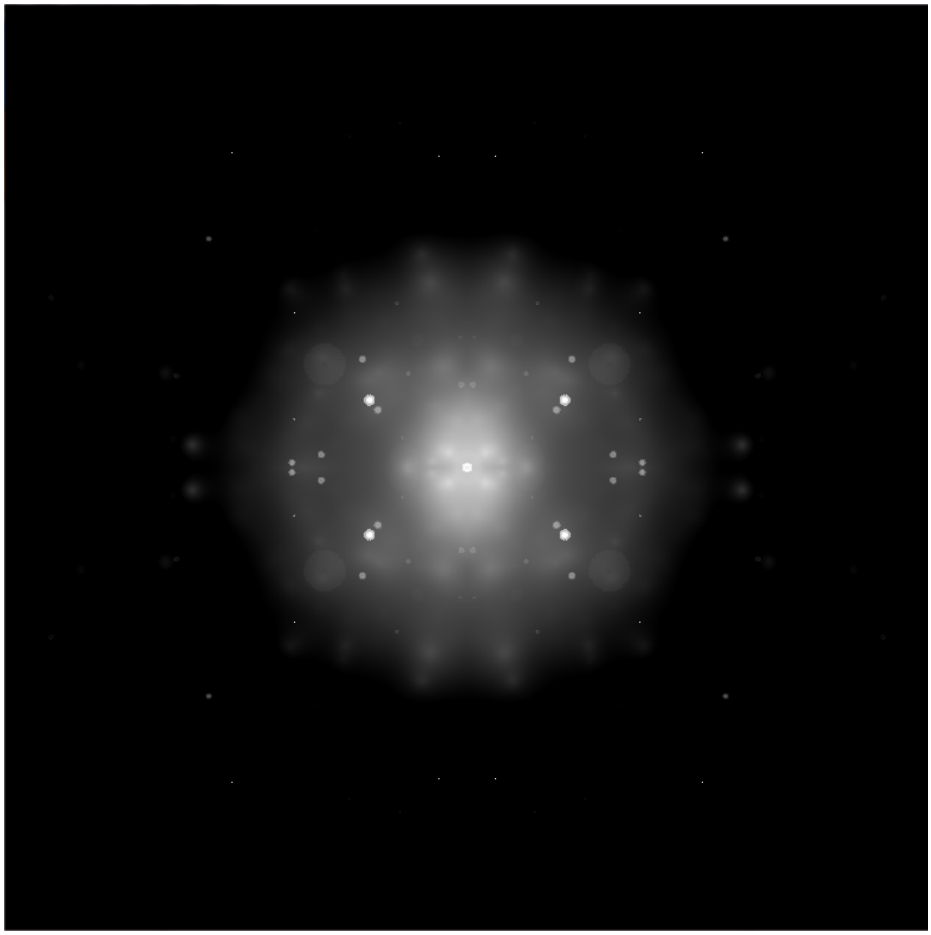

Figure 26: Coherent scatter at image plane for FTO.

The simulations to obtain the coherent scatter were performed using the radiographic tally, capturing the scattered radiation by examining individual monoenergetic and truncating the particles that lost energy due to Compton scatter with the CUT card. These individual simulations were performed over the energy range of 0.5 to 20 MeV. The results were then combined using the initial bremsstrahlung spectrum to obtain the final, single scatter coherent image. This result is presented in Figure 26, which obviously shows some correlation to the FTO object. Unfortunately, to get good statistics (notice the significant amount of noise in the image), the MCNP runs become prohibitively long. Coherent scatter does not occur often enough to provide good statistics in a lengthy full electron/neutron Monte Carlo transport code run. To address the noise in the image the BIE was utilized to create a symmetric image and using the BIE to smooth out the image by creating a symmetric image.

It is also possible to use Hubbell form factors [20] to estimate the coherent scatter kernel. This has been performed and combined using the source energy spectrum.

Correlated Scatter Reconstruction

As previously discussed, an objective of this research is to build a physics based general scatter model based upon the MCNP simulations that may be implemented into the BIE. To this end, it is seen that the scatter at the image plane is composed of the following constituent elements:

- Compton scatter
- Correlated Compton scatter
- Coherent scatter
- Scene scatter from the return of photons from materials not incorporated (except GRC and CV) into the model but present (the ground, extraneous shielding at DARHT, borated concrete)

The Compton scatter has been shown to be very flat due to both the distance of the predominant scattering source from the image plane and the large number of scatters that take place in the object due to the large areal mass. The correlated Compton scatter attributed to the interaction of the direct radiation with the materials in close proximity to the image plane produces a blurred image of the direct signal. Furthermore, the relative fraction of this component is proportional to the areal mass of the object. Using the BIE, one may optimize a model depicted below that allows both the magnitude of the correlated Compton scatter and blur kernel to be determined seen in Figure 27. The red boxes indicate the two scalar variables and the Bennett function that are being optimized on using the 4 plates FTO MCNP Compton scatter data to compare the reconstruction to. The direct scatter, object scatter, and total scatter are found using MCNP and the blur kernel is solved for. The BIE optimizes on the scalars and the blur kernel to make an image as close to the MCNP total scatter image as possible. Once this is done, the blur kernel is

no longer optimized on in subsequent calculations, but the scalar variables are optimized each time the areal mass is changed.

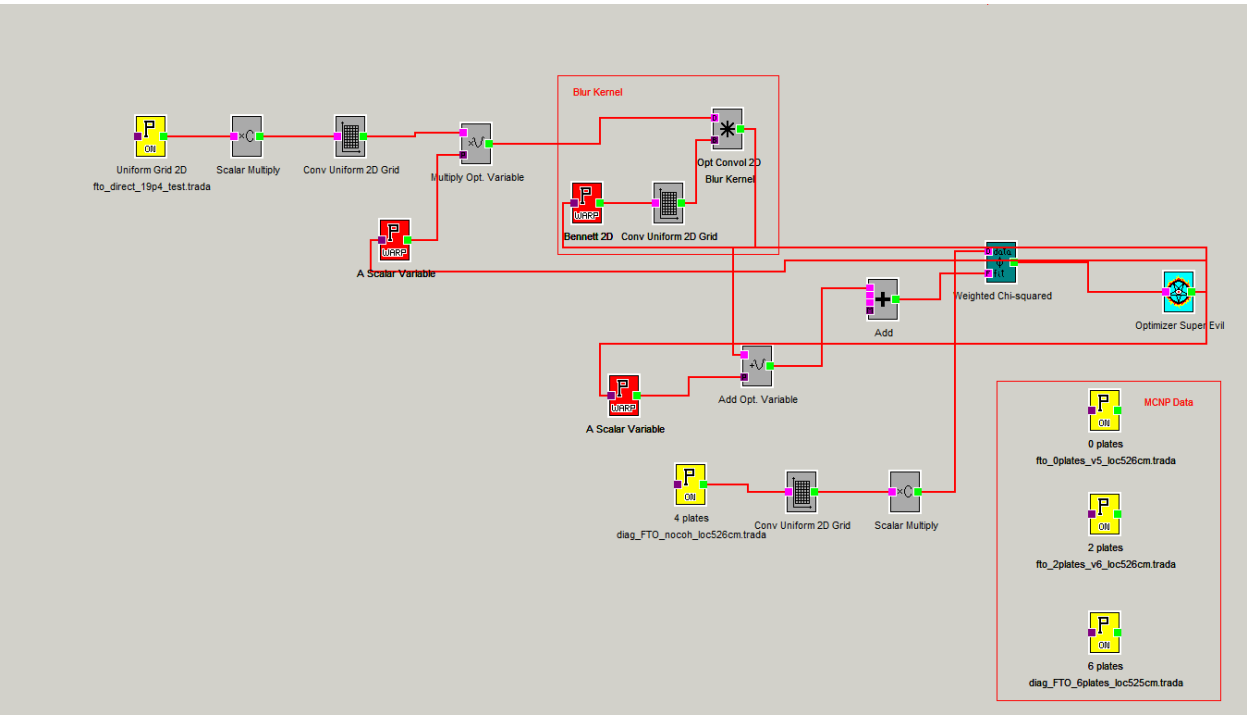

Figure 27: BIE model of correlated Compton scatter blur.

The result of using the BIE to solve for the blur kernel is depicted in Figure 29.

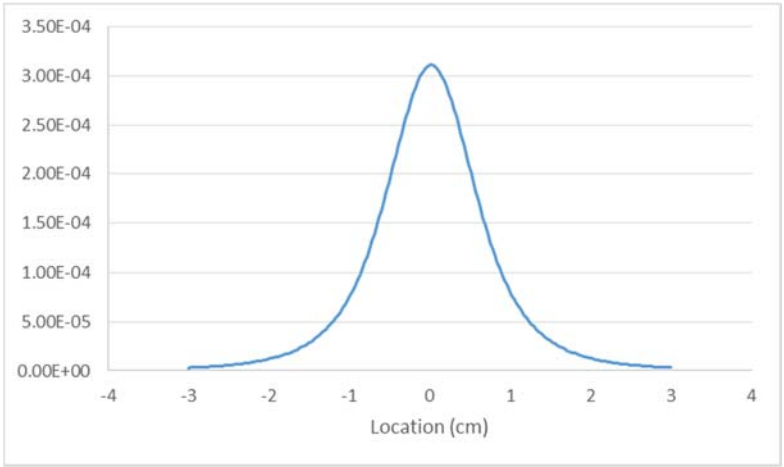

Figure 28: Correlated scatter blur kernel found using FTO with 4 plates.

The aforementioned modeling of the correlated Compton scatter was performed using the FTO with 4 plates and then examined on additional FTO objects using a number of different plates. These results are presented in Figure 29, Figure 30, Figure 31, and Figure 32.

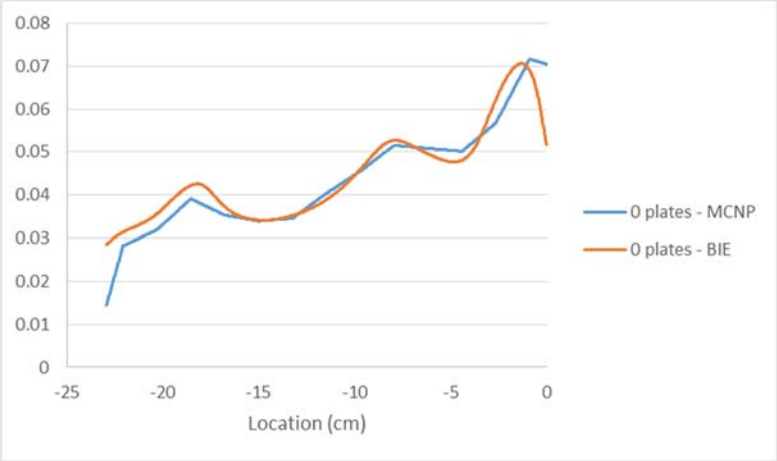

Figure 29: BIE reconstruction of total scatter field of FTO with 0 plates using scatter blur kernel.

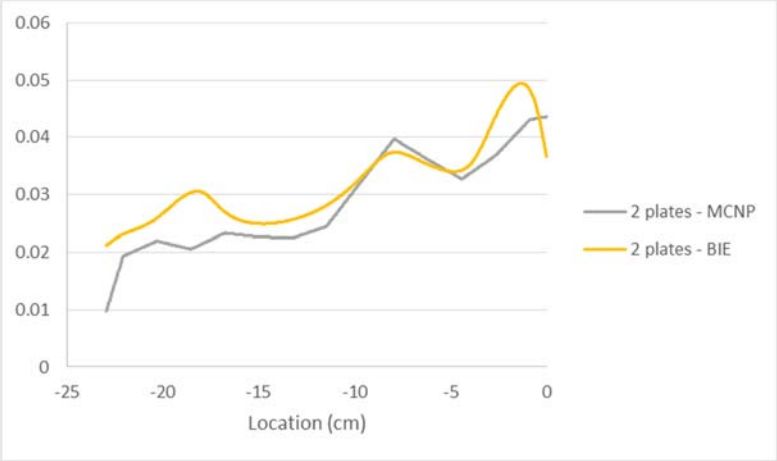

Figure 30: BIE reconstruction of total scatter field of FTO with 2 plates using scatter blur kernel.

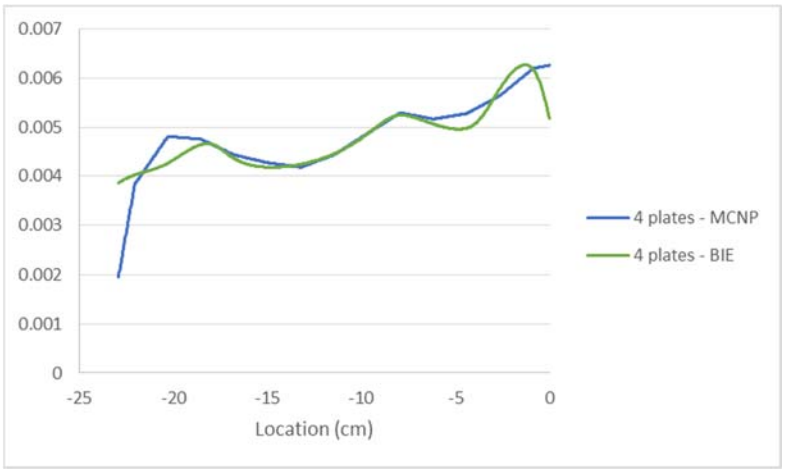

Figure 31: BIE reconstruction of total scatter field of FTO with 4 plates using scatter blur kernel.

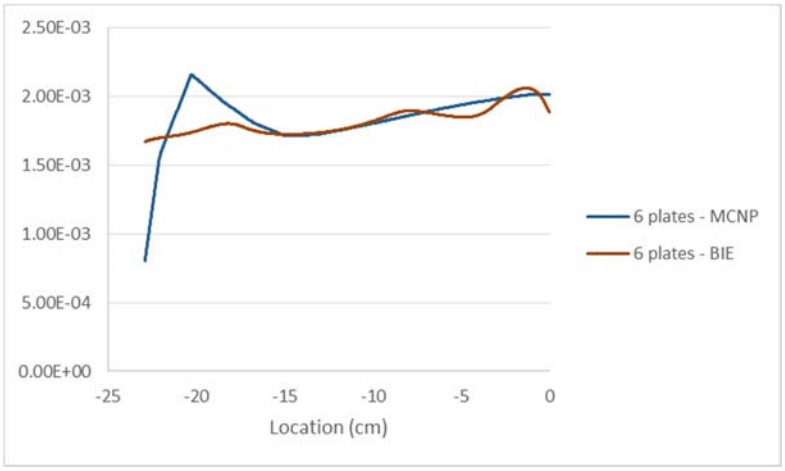

Figure 32: BIE reconstruction of total scatter field of FTO with 6 plates using scatter blur kernel.

Examination of Figure 29, Figure 30, Figure 31, and Figure 32 illustrate that a simple convolution can actually produce a scatter field that is very close to the calculated scatter field, even though the areal mass is changing quite significantly (with ~190 g/cm^2 with 0 plates to ~300 g/cm^2 with 6 plates). In a similar manner the magnitude and blur kernel for the coherent scatter may be obtained using the BIE.

Finally, a model for the scene dependent scatter may be developed. However, since the scene scatter is more difficult to predict since it depends on the amount of scatter coming off the object (which changes depending on the areal mass) and how much of it scatters back into the field of view off the enclosure. This is more difficult to predict and would need a high order polynomial to capture the details of this scatter component. As will be investigated in this research, the use of high order polynomials to represent scatter may introduce errors into the reconstructed density field due to the fact that the density is not truly separable from the scatter field. Consequently, to minimize this separability issue the model for the scene scatter will utilize only a linear scatter

field. Furthermore, the scene scatter will be combined with the Compton scatter and be represented with a linear model in both x and y i.e. bilinear. The constituent elements of the scatter may then be combined and represent the total scatter to be added to the direct image.

The ratio of the scalars that were found through optimization in the BIE are shown in both Figure 33 and Figure 34. It can be seen that as areal mass increases, the correlated Compton scatter relative to the object scatter decreases. This is because there will be more object scatter just due to the larger areal mass, and there will be less direct that reaches the near detector materials and interacts to produce a correlated scatter image. In Figure 33, the ratio is plotted with respect to the overall scatter-to-direct ratio

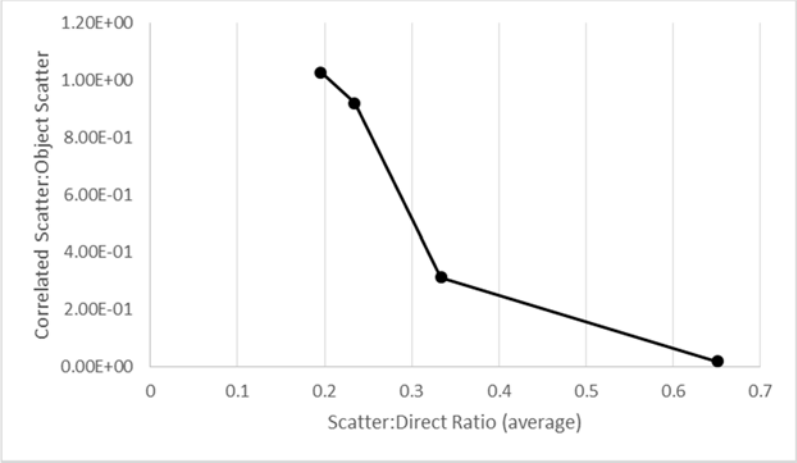

Figure 33: The ratio of correlated scatter to object scatter depending on the overall scatter-to-direct ratio.

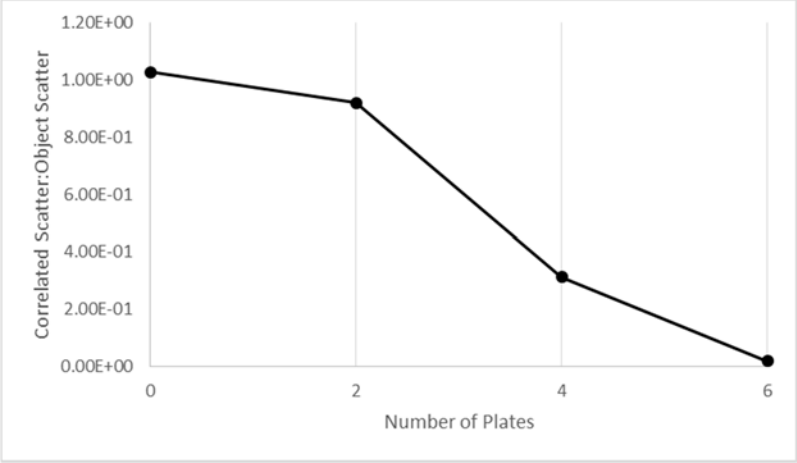

Figure 34: Ratio of correlated scatter to object scatter with respect to number of plates surrounding FTO.

Possible Improvements to Explore

It is possible to model the FTO using a physics based scatter model. Furthermore, the reason for the departure of the inferred blur obtained using the Rolled Edge and AFT along with demonstrating the general characteristics of scatter at DARHT II were determined. It is now possible to utilize this information to make recommendations to minimize the impact of some of the detrimental effects to allow for more accurate and robust density reconstructions. One of the insights gained by this research is the importance of removing the near field materials which create an additional scatter mechanism which is correlated with the direct signal and cannot be modeled by a constant. Research on the replacement of these materials to minimize this effect are ongoing.

Compton Spectrometry Modeling

Measurement of the photon energy spectrum presents a significant challenge due to the very high radiation environment present at DARHT as well as the desire to measure spectra during all four accelerator pulses. A magnetic Compton spectrometer has recently been utilized to measure the energy spectrum on DARHT Axis 1 and is planned for Axis II. The magnetic Compton spectrometer is ideally suited to measure the photon spectrum in DARHT's high radiation environments.

A magnetic Compton spectrometer works by measuring the Compton electron that is scattered when a photon from the source interacts with a converter target (see Figure 8). The electrons are swept into the detector while the remaining photons pass by the detector. By considering Compton energy angle relations, Klein-Nishina cross-sections, and scattering and energy loss of electrons (multiple Coulomb scattering), it is possible to relate the kinetic energy spectrum of the electrons measured by the spectrometer to the initial photon spectrum [25].

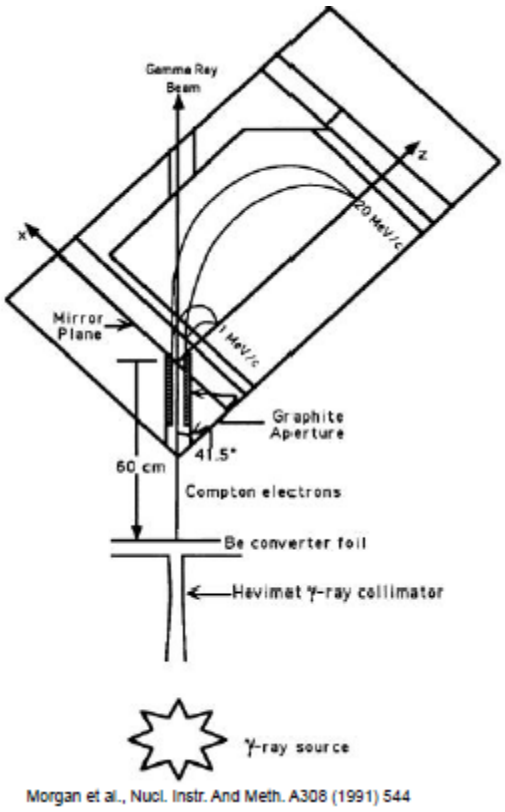

Figure 35: Simple schematic of a Compton spectrometer [26].

Previously, the determination of the photon spectrum from the electron distribution on the focal plan was performed using either an empirically determined sensitivity function to convert electron intensity to photon intensity or by using a line-spread function technique (REFS). While these approaches yielded reasonable estimates of the photon energy spectra as may be observed in Figure 36 the approximations introduced in these methods did not provide sufficient accuracy for the present work.

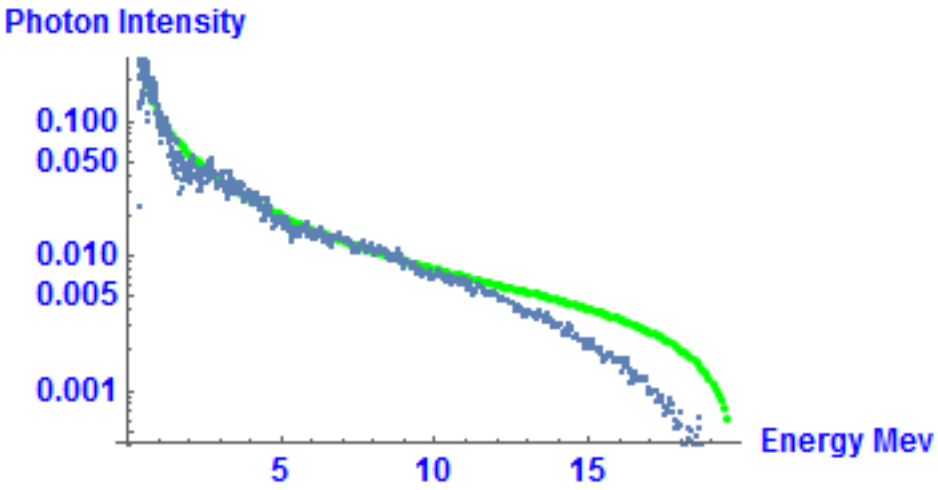

Figure 36: Comparison of simulated intensity (green) and actual data (blue) of 19.4 MeV DARHT shot collected on Compton spectrometer and using previous methodology to reconstruct spectrum.

A new method has been recently developed to de-convolve the electron position on the focal plane into the incident photon energy with much better accuracy. This method relies upon developing a response matrix whereupon the incident source photon spectra may be obtained from the experimentally measured electron intensity on the focal plane without the necessity for any approximations regarding multiple Compton scattering, pair production, or multiple Coulomb scattering. The MCNP calculations are performed by impinging monoenergetic photons onto the Compton convertor target and utilizing the magnetic field capability of MCNP via the BFLD card. An example of the resultant electron distribution on the focal plane is presented in Figure 37.

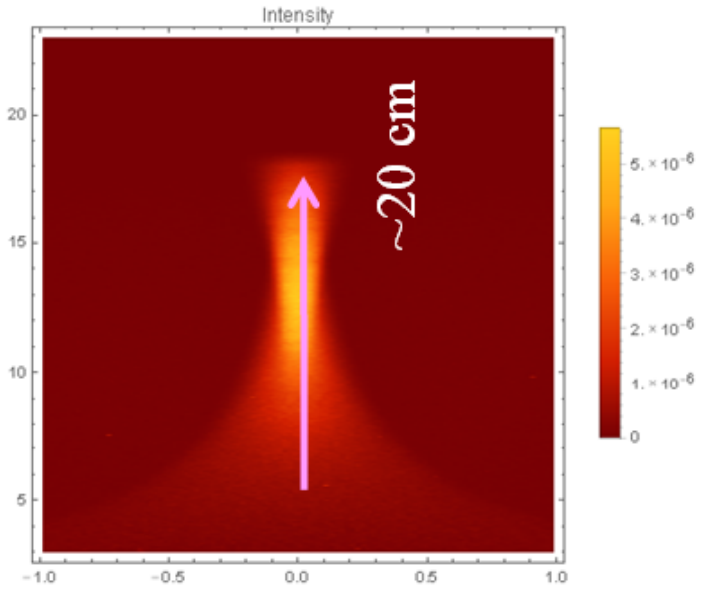

Figure 37: MCNP simulation of electron distribution on the focal plane.

As may be observed from examination of Figure 38 the monoenergetic photon incident on the convertor target produces a long tail of electrons that can contribute to the signal at all other positions. That is, unlike the previous methods which largely ignored the contribution of the tail this method explicitly accounts for the tails. The tails are largely due to the distributed electron source produced inside the Compton convertor and the multiple Coulomb scattering. Figure 38 shows the extent of the tail for a wide range of monoenergetic source photons.

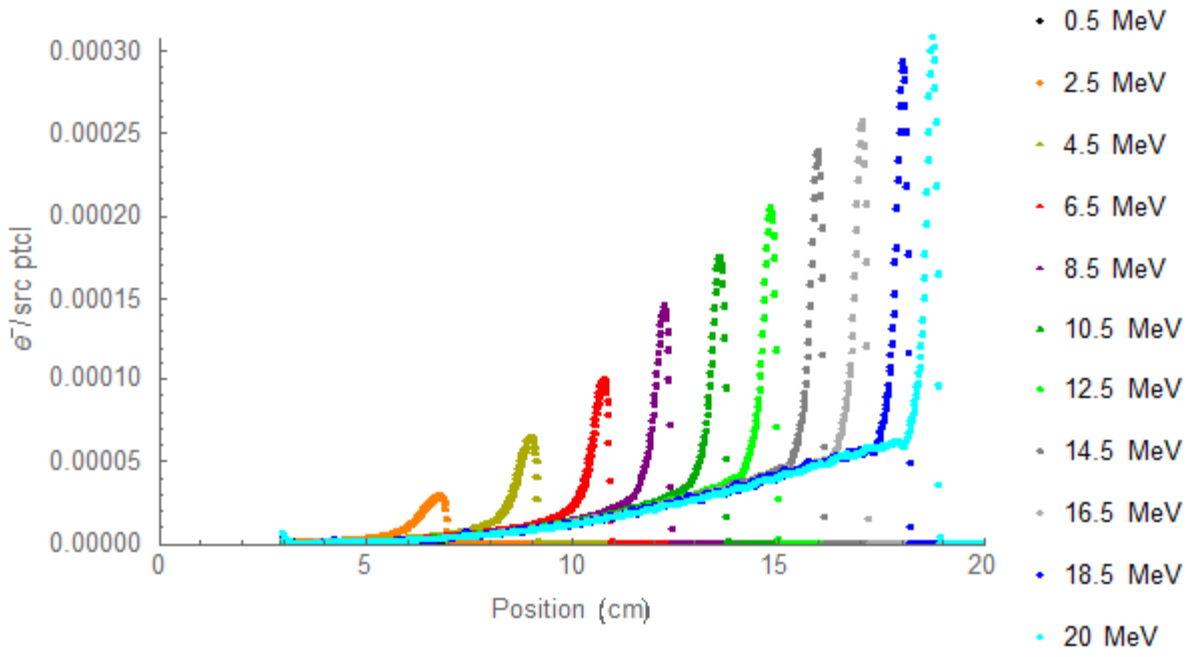

Figure 38: Monoenergetic photons impinging on converter target produce electrons measured in Compton spectrometer in MCNP.

Instead of using many assumptions that the previous methodology employed, data from MCNP which includes all processes (multiple scatters, pair-production, etc.) can be used. A linear combination of the data can be solved for to produce the photon intensity versus energy data that is wanted from the electron intensity versus position data that is measured. This is a simple linear programming problem as seen in equation 12.

$$R \cdot \vec{s} = \vec{m} \qquad (12)$$

$\vec{s}$ is the unknown photon spectrum, what is being solved for. $\vec{m}$ is the electron distribution on the focal plane, the data that is collected by the Compton spectrometer. R is the response matrix which is developed from the MCNP simulations of monoenergetic photons impinging on a Compton convertor and mapped to a focal plane. It is a matrix of electron intensities based on the energy and position as seen in equation 13.

$$R = \begin{bmatrix} I(E_1, x_1) + I(E_2, x_1) + \cdots + I(E_n, x_1) \\ I(E_1, x_2) + I(E_2, x_2) + \cdots + I(E_n, x_2) \\ \vdots \\ I(E_1, x_n) + I(E_2, x_n) + \cdots + I(E_n, x_n) \end{bmatrix} \qquad (13)$$

Using the new method, an improved agreement between the DARHT Axis I data and the MCNP model of the bremsstrahlung spectra emitted from the 1 mm convertor target may be observed in Figure 39. The error in the experimental data is largely attributed to both the uncertainty in the focal position as well as the counting statistics. An error associated with the MCNP data method has also been calculated, it is very small and cannot be seen in Figure 41.

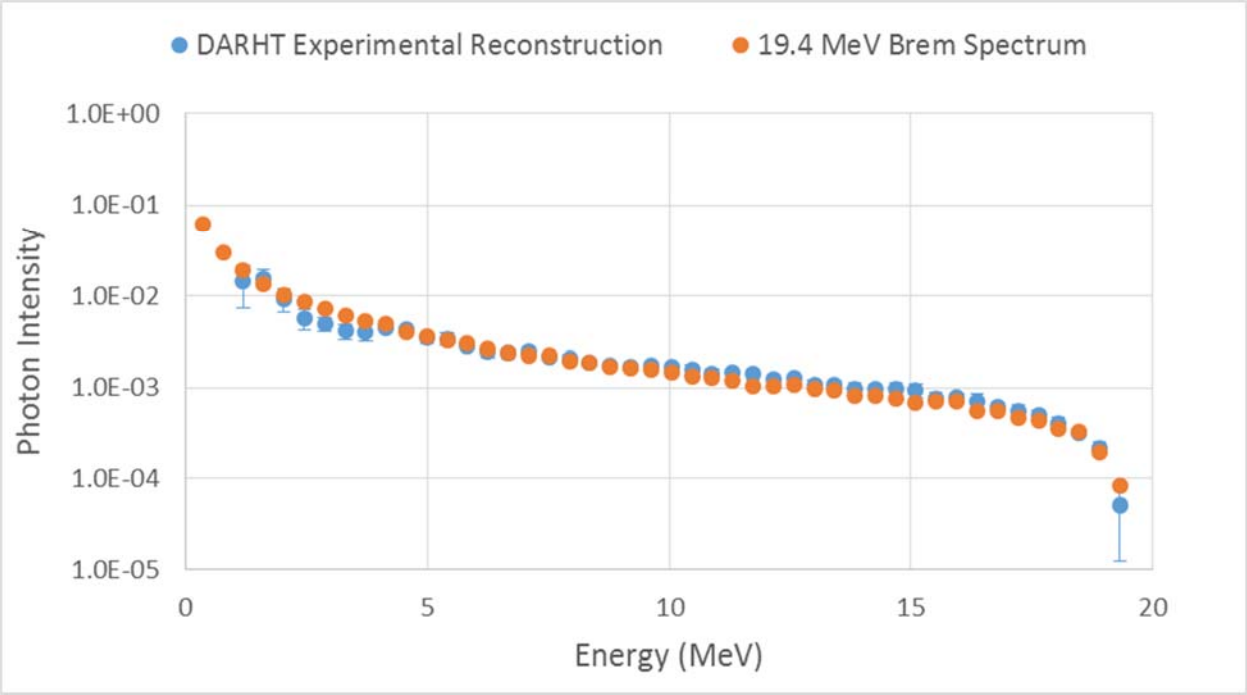

Figure 39: Comparison of DARHT experimental spectrum with MCNP simulated spectrum of 19.4 MeV endpoint electron.

This same approach will be utilized to unfold the DARHT Axis II data for the four pulses. Although the initial runtime is significant since each monoenergetic photon must be run and the resolution of the tally is fine, once the response matrix is developed, it can be used for any experiment as long as the Compton spectrometer does not change. This makes this methodology easy to use and practical.

List of Tasks

Tasks (Complete/Incomplete) and Timeline

1) **Make Reduced Geometry Model of DARHT Axis 1 and DARHT Axis II in MCNP.**
   Completed

   Build DARHT model in MCNP using line-of-sight materials and some surrounding materials. The ground and building will be omitted due to prohibitively long runtimes. This reduced model should provide significant insight into the nature of scatter at DARHT.

2) **Describe DARHT Source in MCNP.**
   Completed
   DARHT uses an electron beam to produce bremsstrahlung X-rays which are used to image the object of interest. There is a finite source size with an associated PSF that can

be inferred from experimental measurements of the spot. The energy spectrum of the spot can be determined from an MCNP run which impinges electrons onto the target material found at DARHT (W or Ta). Finally, there is an associated angular distribution of the photons coming off the target. This is generally thought to be around 2.55°. The source impacts the transmission and scatter significantly and must be implemented as accurately as possible.

3) **Analyze variety of static objects in MCNP (FTO, rolled edge, AFT).**
Completed
Different static objects provide data for different areas of analysis experimentally. The rolled edge and AFT are frequently used for source blur calculations whereas the FTO is used to infer scatter fields. These same objects should be run in MCNP to provide a control. These runs will allow source blur and scatter to be analyzed and determine if the current methods of analysis are accurate or need improvement.

4) **Compare BIE direct results with MCNP direct results.**
Completed
The BIE can provide direct transmission results in seconds whereas MCNP takes hours to provide a converged high-resolution direct transmission result. If possible, it would be desirable to be able to do all direct runs in the BIE, but this needs to be validated by MCNP. If an identical model in MCNP and the BIE match up, it is no longer necessary to run direct transmission runs in MCNP.

5) **Determine Spectra Going Across Plane (affects the detector response).**
Completed
The spatial energy spectrum needs to be determined in order to see how much change across the detector plane there is in the spectrum. The detector (scintillator) is very energy dependent and if the energy spectrum of the scatter or direct fields changes drastically across the plane this will be magnified by the detector response. This needs to be analyzed using MCNP.

6) **Using Results, Make Generalized Model of Scatter that Can Be used without running MCNP for specific case.**
Completed
For the scatter results to be of the most use, it is desirable to have some generalized model that allows analysis to be done purely in the BIE when small changes are made to the experiment. This will allow quick, versatile modeling without relying on large amounts of processors to perform the same task.

7) **Compare MCNP model results and generalized model results with actual DARHT experimental data.**
Incomplete

MCNP model results with need to be compared and validated to DARHT experimental data to show its true usefulness.

8) **Look at improvements that can be made to current DARHT geometry (removal of near detector materials, change in collimation).**

In process

If the DARHT computational model or DARHT experimental set up are less than optimum for analysis and the scatter field, changes should be suggested to improve the system.

9) **Investigation of bounding cases for hydrodynamic effects on radiation transport at DARHT Axis II.**

In process

Of interest is the effect of hydrodynamic movement on the photon spectrum at DARHT Axis II. CTH will be loosely coupled with MCNP in order to determine spectral effects. MCNP will be used to determine the energy deposition in the target material. This can then be inputted into CTH which will output the density and temperature of the target and plume coming off the target.

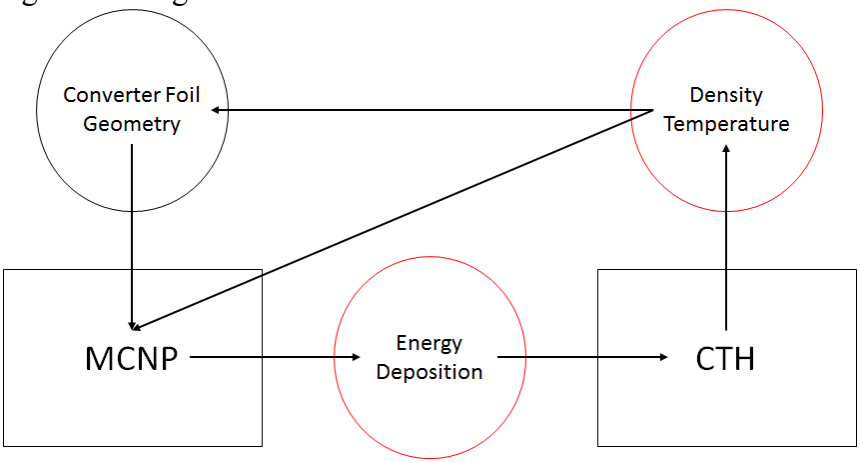

Figure 40: Flow chart of loose coupling of MCNP and CTH.

10) **Other Work (Compton spectrometry)**

Complete

Some other areas not directly related to this research may be added. Compton spectrometry experiments and modeling have been performed and some improvements made to current modeling techniques. These experiments also provide insight into the spectra at radiographic facilities such as DARHT and CYGNUS.

11) **Write up**

Incomplete

LANL will require that a review of the dissertation is performed to ensure that there is no sensitive information in the document. The dissertation must be submitted and given an

LA-UR number. Due to the length of the dissertation, this could take around a month to complete.

Citations

1. "Stockpile Stewardship Program Quarterly." NNSA. https://nnsa.energy.gov/ourmission/managingthestockpile/sspquarterly
2. "Comprehensive Nuclear Test-Ban Treadty (CTBT)." US Department of State. https://www.state.gov/t/avc/c42328.htm
3. C. Rose. "DARHT: An Overview." Colorado Springs IEEE Chapter. LA-UR-13-27538. Sept. 27, 2013.
4. S. Watson and D. Bowman. "Techniques for Estimating Scatter Background." DARTH Technical Notes. LA-UR-06-1634. 2006.
5. "Klein-Nishina formula" Wikipedia. https://en.wikipedia.org/wiki/Klein%E2%80%93Nishina_formula Accessed May 1, 2017.
6. "X-ray Production" Radiology Key. https://radiologykey.com/x-ray-production-2/ Accessed May 2, 2017.
7. L. Auditore, R. Barna, etc. "Design of an e-γ converter for a 10MeV electron beam." Proceedings of 2011 Particle Accelerator Conference, NYC. 2011.
8. "Coherent scattering." Radiopaedia. https://radiopaedia.org/articles/coherent-scattering Accessed May 17, 2017.
9. G. Hajdok, J.J. Battista, I.A. Cunningham. "Fundamental x-ray interaction limits in diagnostic imaging detectors: Spatial resolution." American Association of Physicists in Medicine. Medical Physics 35(7):3180-93. July 2008.
10. M. Gittings, R. Weaver, M. Clover, etc. "The RAGE radiation-hydrodynamic code." Computational Science & Discovery, Volume 1, Number 1. April 9, 2008.
11. M. Berninger, etc. "The physics and validation of the Cygnus radiographic source for Armando." 14TH Biennial Nuclear Explosives Design Physics Conference. LA-UR-03-7780. 2003.
12. S. Nata. "DARHT II option for advanced radiography." Advanced Radiography Meeting at NNSS. LA-UR-11-02623. May 4, 2011.
13. T. Kwan, A. Matthews, P. Christenson, C. Snell. "Integrated system simulation in X-ray radiography." Computer Physics Communications 142. 2001.
14. M. Burns, etc. "Status of the DARHT Phase 2 Long-Pulse Accelerator." LA-UR-01-3810. 2001.
15. S. Watson, C. Lebeda, A. Tubb, M. Appleby. "The Design, Manufacture, and Application of Scatter Reduction Grids in Megavolt Radiography." LA-UR-99-1111. 1999.
16. D. Trubey, etc. "Reactor Shielding for Nuclear Engineers." N.M. Schaeffer. US Atomic Energy Commission. 1973.
17. P. Volegov, etc. "Neutron source reconstruction from pinhole imaging at National Ignition Facility." Review of Scientific Instruments 85. January 2014.
18. C. Tomkins, M. Klasky. "DARHT Technical Note No. 464." LA-UR-07-5486. Sept. 11, 2008.

19. Y. Harima. “An Historical Review and Current Status of Buildup Facto Calculations and Applications.” Radiation and Physical Chemistry. Vol. 41, No. 4/5. December 1992.
20. J. Hubbell, W. Veigele, E. Briggs, R. Brown, D. Cromer, R. Howerton. “Atomic Form Factors, Incoherent Scattering Functions, and Photon Scattering Cross Sections.” Journal of Physical Chemistry. Vol. 4, No. 3. 1975.
21. S. Watson, D. Bowman. “Techniques for Estimating Scatter Background.” LA-UR-06-1634. 2006.
22. D. Trubey. “New Gamma-Ray Buildup Factor Data for Point Kernel Calculations: ANS-6.4.3 Standard Reference Data.” Radioation Shielding Information Center. ORNL/RSIC-49. September 1988.
23. “CTH Capabilities.” Sandia National Laboratories. http://www.sandia.gov/CTH/Capabilities-leftnav-level1_js.html. Accessed August 21, 2017.
24. Dave Crawford. “CTH Course Notes.” Sandia National Labs. December 2014.
25. R. Morneau, M. Klasky, M. Espy, etc. “A Method to Determine Energy Spectra from Compton Spectrometer Measurements.” LANL. April 20, 2017.
26. A. Gehring, M. Espy, T. Haines, etc. “Measuring x-ray spectra of radiographic sources with a Compton spectrometer.” 4th Joint Meeting of the APS Division of Nuclear Physics and the Physical Society of Japan. Oct. 6-11, 2014. LA-UR-14-27761.
27. “H4274 Axis 1 Ray Trace.” Drawing Number 34Y1770880. LA-REL-08-Apr-14.
28. George, M.J., K.H. Mueller, R.H. O’Connor, and R.G. Schrandt. “The Use of the Monte-Carlo Method to Simulate High-Energy Radiography of Dense Objects”. United States. LA-11727-MS. January 1990.
29. C. Lebeda. “Memorandum: Blast Shield Scatter Functions.” LANL.
30. J. O’Malley and S. Quillin. “Collaborative scattering experiments at LANL Microtron facility: experimental proposal notes.” Atomic Weapons Establishment. April 1997.
31. C. Lebeda. “Memorandum: Graded Collimator Studies.” LANL. July 1996.
32. M. George and R. O’Connor. “Continued Calculations of Radiographic Scattering Using the Monte-Carlo Method.” LANL. November 1991.
33. M. George and L. le Dain. “A Joint Los Alamos – French Study of Photon Scattering Using the Monte Carlo Method.” December 1992.

Appendix A

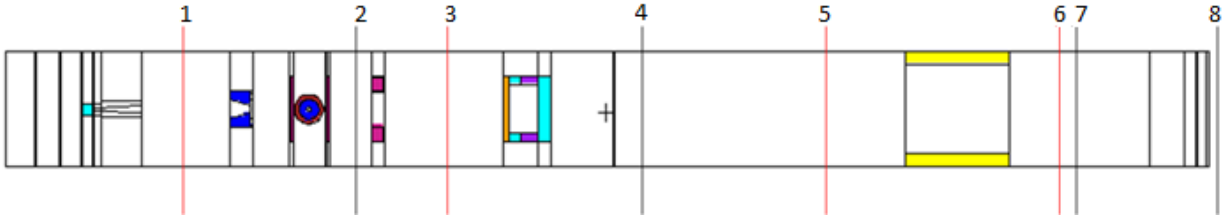

Figure 41: MCNP model of DARHT with red and black lines separating zones for other plots.

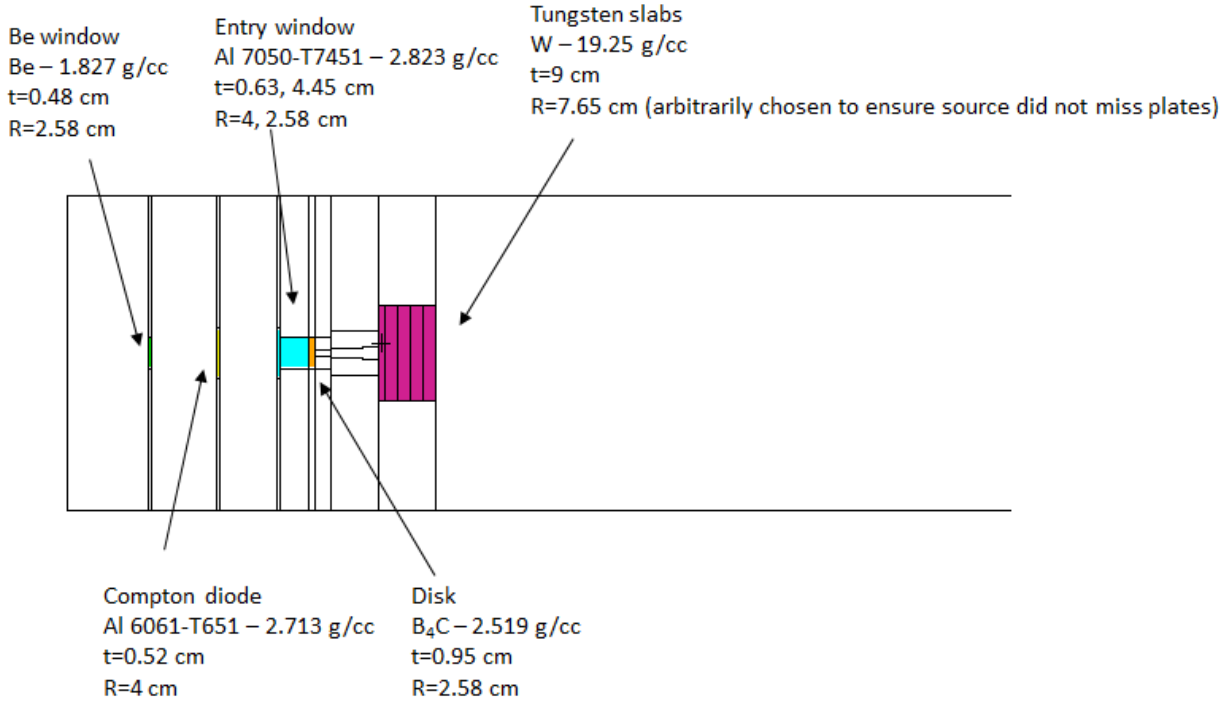

Figure 42: Enlarged plot of area before 1 (seen in Figure 41) for the AFT which has material in the bull nose.

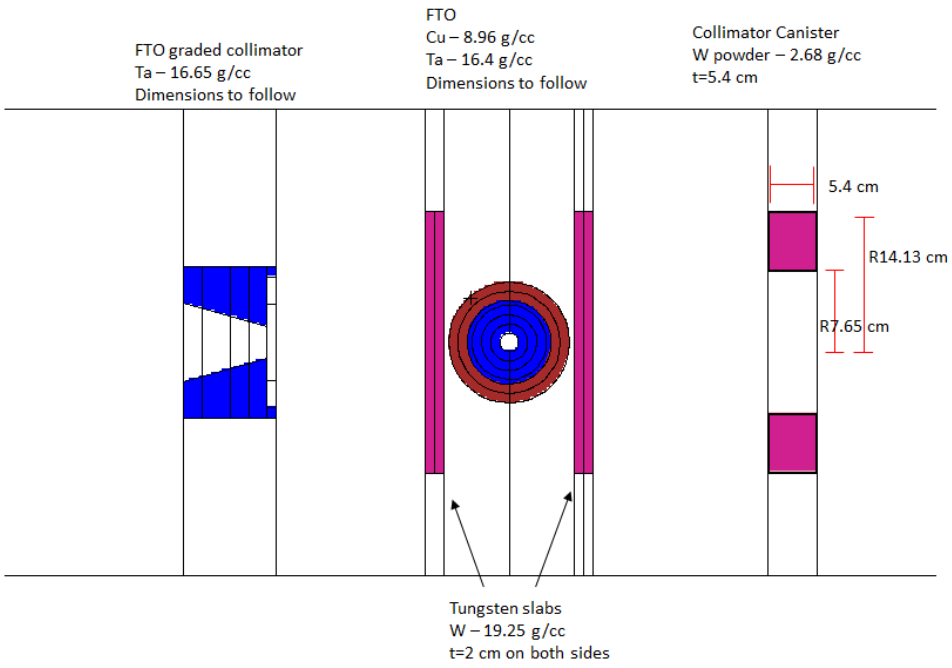

Figure 43: Enlarged plot of area between 1 and 2 (seen in Figure 41) for the FTO.

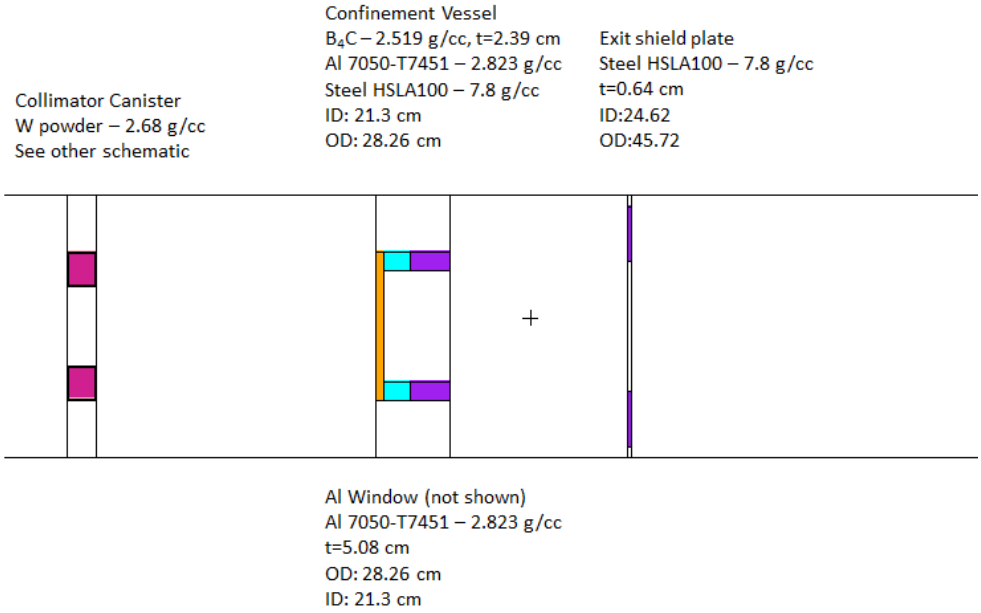

Figure 44: Enlarged plot of area between 2 and 4 in Figure 41 for FTO, AFT, etc.

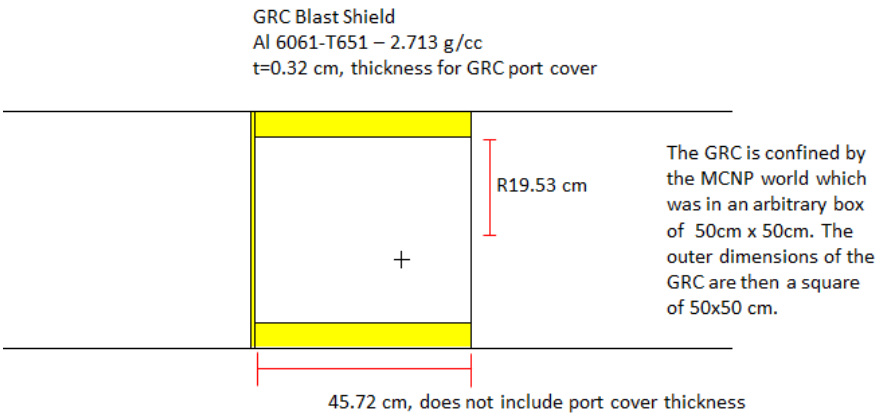

Figure 45: Enlarged plot of area between 5 and 6 in Figure 41 for FTO, AFT, etc.

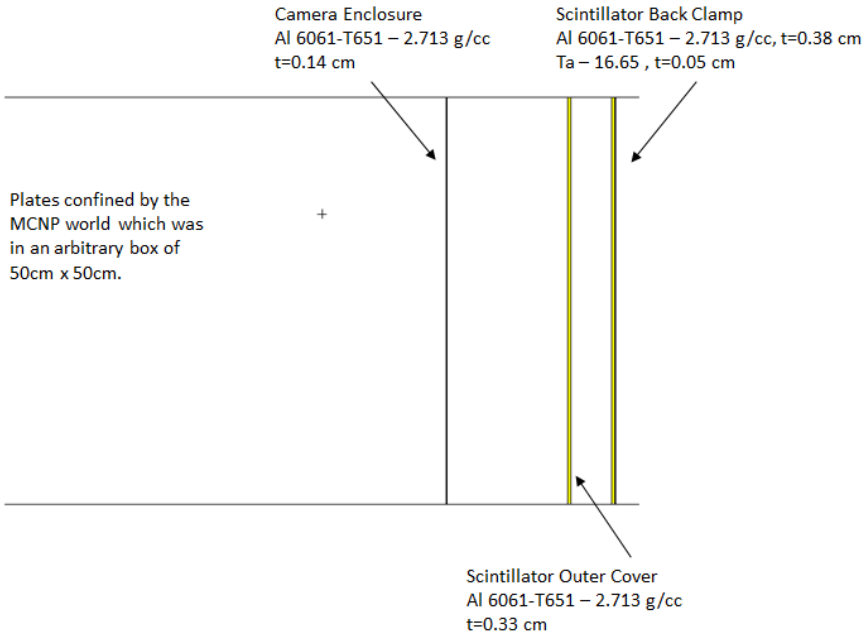

Figure 46: Enlarged plot of area between 7 and 8 in Figure 41 for FTO, AFT, etc.

Figure 47: Ray trace of DARHT Axis I [27].

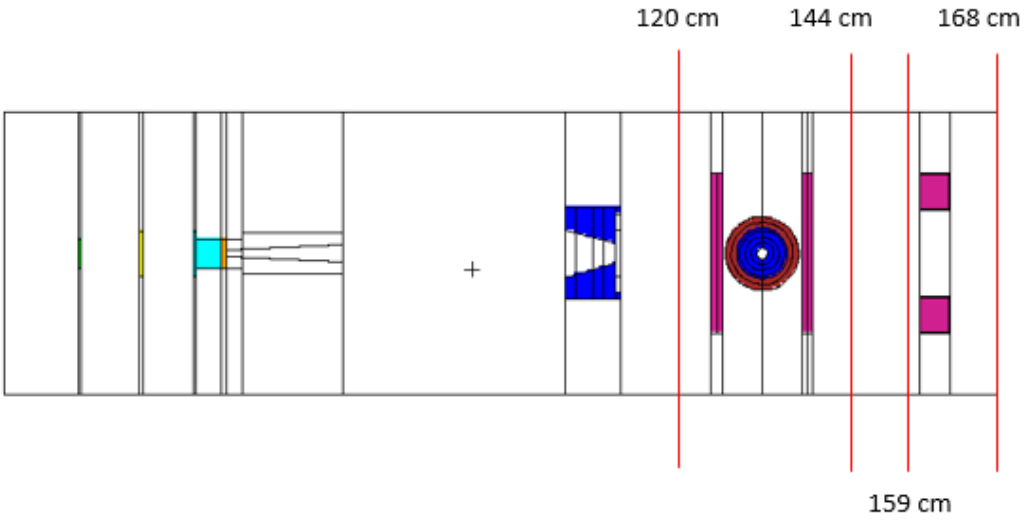

Figure 48: Locations of detectors in DARHT MCNP runs.

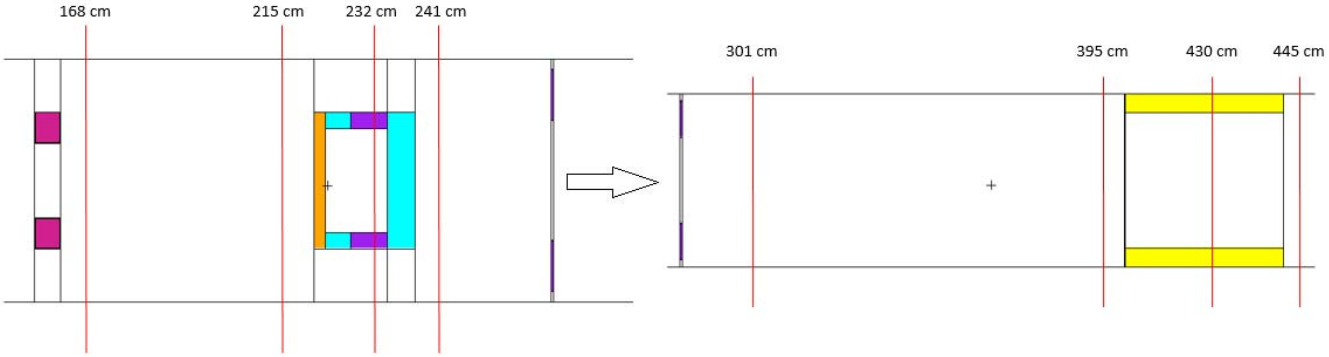

Figure 49: Locations of detectors in DARHT MCNP runs.

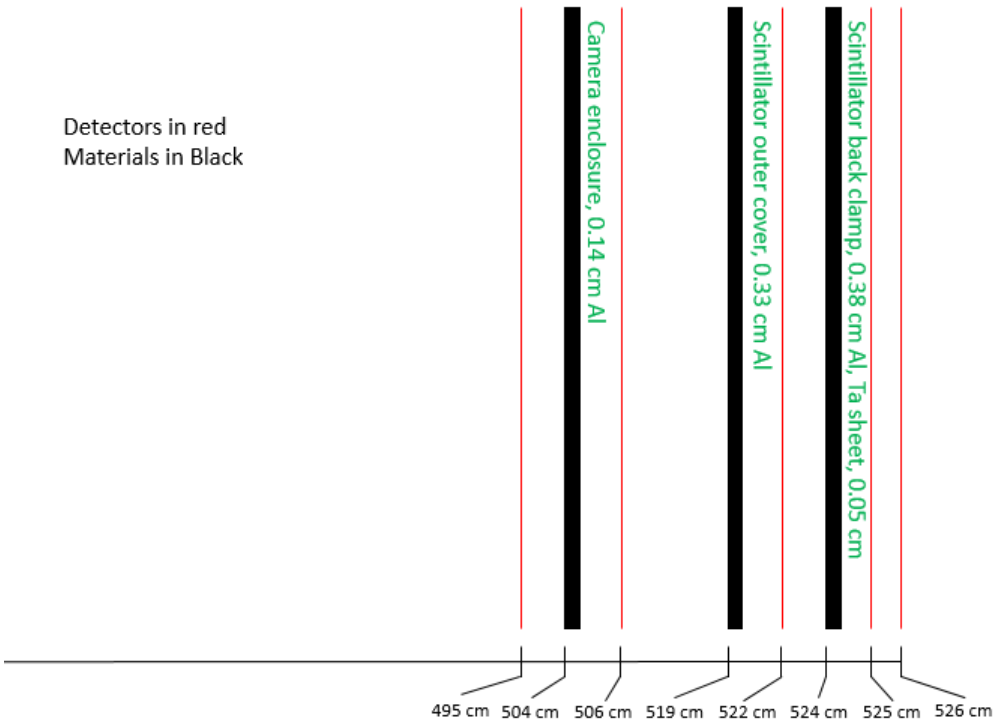

Figure 50: Detector locations in DARHT MCNP runs.

Appendix B

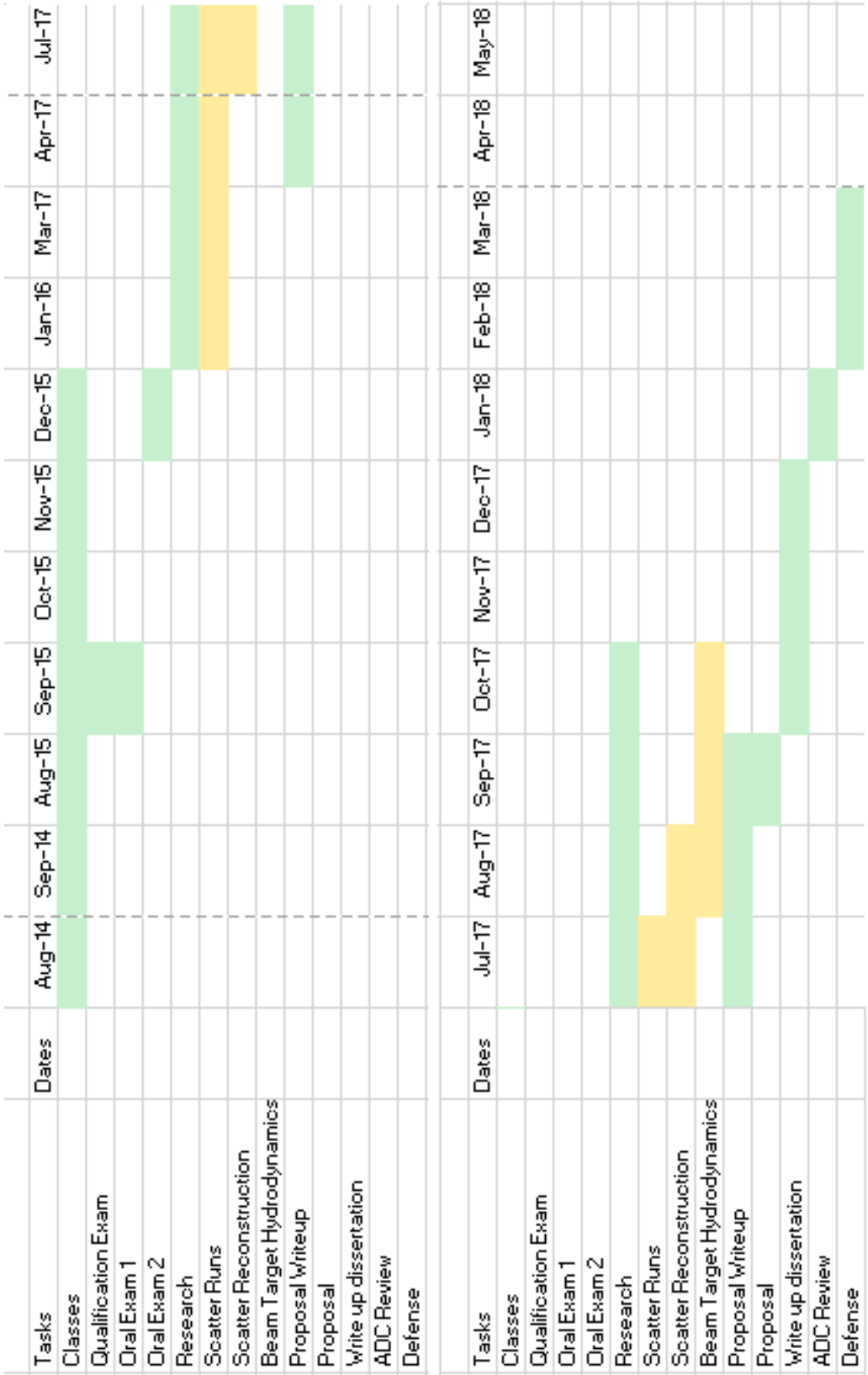
Tasks
Dates
Aug-14
Sep-14
Aug-15
Sep-15
Oct-15
Nov-15
Dec-15
Jan-16
Mar-17
Apr-17
Jul-17
Classes
Qualification Exam
Oral Exam 1
Oral Exam 2
Research
Scatter Runs
Scatter Reconstruction
Beam Target Hydrodynamics
Proposal Writeup
Proposal
Write up dissertation
ADC Review
Defense
Tasks
Dates
Jul-17
Aug-17
Sep-17
Oct-17
Nov-17
Dec-17
Jan-18
Feb-18
Mar-18
Apr-18
May-18
Classes
Qualification Exam
Oral Exam 1
Oral Exam 2
Research
Scatter Runs
Scatter Reconstruction
Beam Target Hydrodynamics
Proposal Writeup
Proposal
Write up dissertation
ADC Review
Defense